University of Zurich[UZH]

ETH zürich

Symmetry Breaking in Quantum Cascade Lasers with Circular Cavities

Master's Thesis

Réka-Eszter Vass

Supervised by
Prof. Dr. Johan Chang

Supervised by
Prof. Dr. Jérôme Faist
Ina Heckelmann

Zürich
August 2023

Abstract

The primary goal of this thesis is to investigate the mechanisms and underlying phenomena of symmetry breaking in quantum cascade lasers embedded in circular cavities. In particular, we studied the importance and nature of backscattering.

The efforts in addressing the challenges associated with ring quantum cascade lasers, such as their low output power and bistable behavior, are also discussed. A specific emphasis is placed on investigating the potential of anti-reflection coatings to influence and control the spontaneous preferential emission direction of these devices.

While the results show some degree of control, further study is needed to unlock the full potential of ring quantum cascade lasers. Because, it is of crucial importance for any practical application and integration of the ring quantum cascade lasers, like single-mode sources for high-resolution absorption measurements, and ultrastable frequency comb sources in dual-comb spectroscopy, to be able to drive the lasing direction.

Contents

Chapter 1

Introduction

The infrared spectral range, spanning between the visible and microwave regions of the electromagnetic radiation spectrum, can be divided roughly into three subregions, each with distinct physical properties and applications.

Above the visible wavelengths, the near-infrared range can be found between 800 nm and 2.5 μm, which is often used in optical telecommunications and remote control technologies [1].

With longer wavelengths between 3 μm to 25 μm, the mid-infrared range is relevant for spectroscopic applications as it coincides with fundamental rotational-vibrational absorption bands of many molecules, which exhibit strong resonances in this region. For example, the characteristic absorption line intensity is stronger in the mid-infrared range for many greenhouse gases and pollutants, compared to the neighboring regions, as shown in figure 1.1 [2].

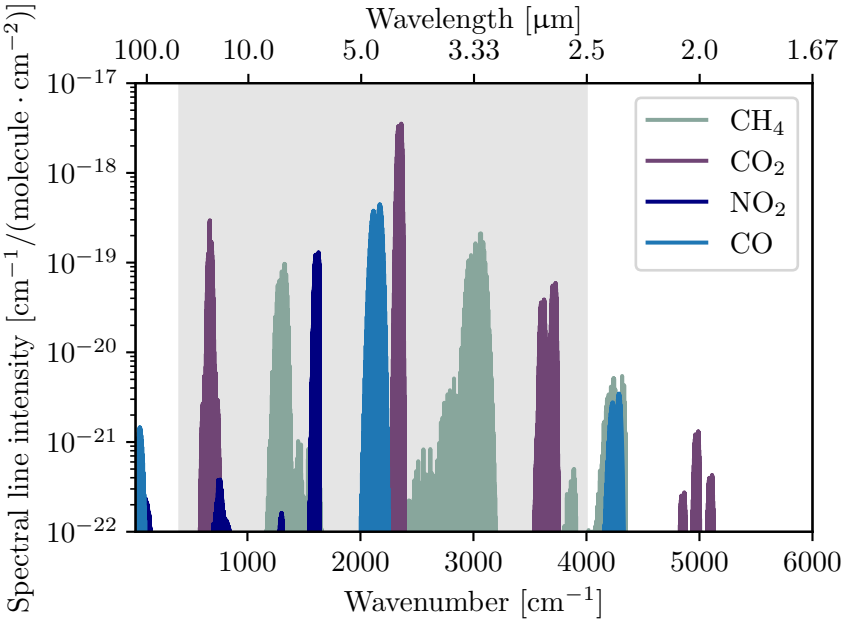

Figure 1.1: Absorption line strengths in the shaded mid-infrared spectral region of different greenhouse gases and pollutants show strong resonances. Source: HITRAN 2020 [2]

The mid-infrared absorption spectrum is specific to each molecule. Hence, this region is referred to as the "molecular fingerprint" region. The rotational-vibrational absorption bands present make the mid-infrared wavelength range attractive for spectroscopic applications, as they allow for the detection of molecules in lower concentrations [3].

Moving from the mid-infrared to even longer wavelengths, from 25 μm to 1 mm, we enter the far-infrared, or the terahertz range, which is associated with thermal radiation and finds use in astronomical applications [4].

In the mid-infrared region of the electromagnetic radiation spectrum, which will be the topic of this thesis, three types of semiconductor laser sources are present, all based on a heterostructure design — namely, the laser diode, the interband cascade laser, and the quantum cascade laser.

Ever since the realization of the first laser device [5] in 1960, different cavity designs and gain mediums were explored. In the case of quantum cascade lasers, until recent years, mostly Fabry-Pérot devices were studied. However, not long ago, quantum cascade lasers were also realized in ring cavities, which show distinct behavior from linear ones. It provides a platform for generating both ultrastable frequency combs [6, 7] and purely single-mode devices [8].

Here, we will focus on mid-infrared quantum cascade laser devices embedded in circular cavities, with a particular interest in their symmetry-breaking phenomena.

In chapter 2, we will briefly introduce the quantum cascade laser and discuss how ring cavities differ from Fabry-Pérot devices. Furthermore, we discuss the necessary theory for designing anti-reflection coatings, which then can be applied to the laser facet. Moreover, the measurement techniques used for the optical, electrical, and spectral characterization of ring quantum cascade lasers are also briefly discussed.

Chapter 3 presents a collection of the results in the attempt to enhance the performance of ring quantum cascade lasers and their reliability in the lasing direction choice. The influence of an anti-reflection coating on the laser facet, the connection of the bidirectional regime to the spectrum, and the spectrum of the two counter-propagating directions are discussed. Furthermore, the thermal properties of heterostructure layers used to realize a modified ring design are presented. In addition, a comparison is also included between the ring and egg design, where an optimized curvature of the active region is employed to address the outcoupling efficiency of the devices.

In chapter 4, conclusions are summarized on the symmetry-breaking phenomena of the ring- and egg-shaped quantum cascade lasers and the connection between their main and counter-propagating modes.

Chapter 2

Theory and Methods

2.1 Quantum Cascade Lasers

As mentioned in the introduction, three competing semiconductor laser sources exist in the mid-infrared spectral region. While the laser diode and the interband cascade lasers are based on interband transitions, the photon emission in the quantum cascade laser emerges from intersubband transitions between confined electronic states. Quantum cascade lasers are unipolar semiconductor devices that were first demonstrated in 1994 [9]. They are based on a heterostructure design and are grown by molecular beam epitaxy.

Difference between interband and intersubband transitions

Intersubband transitions are inherently different from interband ones, as illustrated schematically in figure figure 2.1. During an interband transition, the electrons from the conduction band recombine with holes in the valence band of a semiconductor and emit a photon. Therefore, the bandgap, characteristic of the used material, defines the transition energy. While in the intersubband case, the transition energy is adjustable and relies on the heterostructure design.

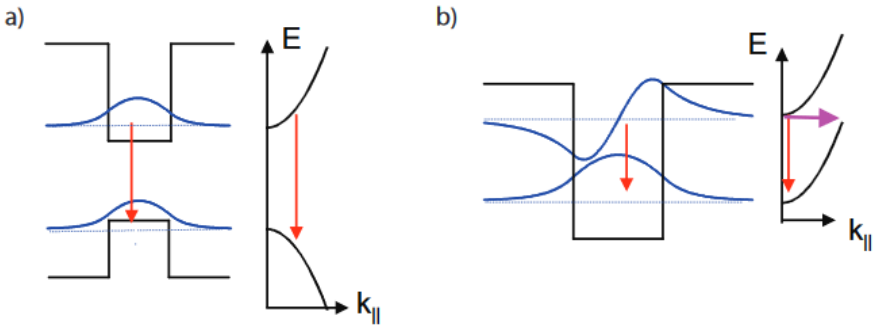

Figure 2.1: Interband and intersubband transitions. Panel a) shows an interband transition between the valence and conduction band of a semiconductor, which exhibits dispersion curves of opposite sign, while panel b) depicts an intersubband transition between confined electronic states in the conduction band of a semiconductor, with identical in-plane dispersion. The figure is reprinted from [10]

By varying the thicknesses of the different semiconductor layers for the quantum wells and barriers in the heterostructure, the electronic energy states can be shifted, and in doing so, the emission wavelength of the device can be tuned using the same material system.

Consequences of the intersubband transitions

Quantum cascade lasers are characterized by a short upper-state lifetime of the gain medium. Since, in the case of intersubband transitions, the energy transfer happens between states within the same band, any elastic or inelastic scattering event with sufficient momentum exchange allows the scattering of an electron from the upper to the lower state. This limits the lifetime of the electron to the picosecond timescale [11], compared to lifetimes of the order of nanoseconds in the case of interband transitions, where radiative processes dominate the transitions along the band gap.

The short upper state lifetime is unique to quantum cascade lasers, as it is a consequence of the intersubband transitions, which are dominated by non-radiative processes, like interface roughness scattering and phonon-assisted transitions. The short upper state lifetime causes fast transport dynamics, which leads to a small optical gain. Therefore significant power is dissipated in the material to induce population inversion.

2.2 Ring Quantum Cascade Lasers

Ring quantum cascade lasers differ majorly in multiple ways from Fabry-Pérot devices. The most obvious difference is the geometry of the active region, as shown in the microscope images in figure 2.2. First, an epitaxial-side down mounted Fabry-Pérot laser is visible on panel a), and then a fabricated, but not mounted ring laser is shown on panel b). The epitaxial-side down and up terms refer to the positioning of the buried active region in the indium phosphide (InP) cladding [12].

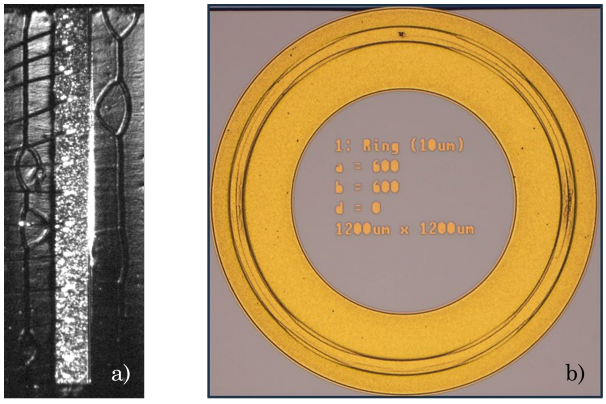

Figure 2.2: Microscope images of lasers with different cavity designs fabricated from the same heterostructure. Panel a) shows an epitaxial-side down mounted Fabry-Pérot device, while panel b) shows an epitaxial-side up ring laser before mounting. In both cases, the heterostructure layers lay parallel to the surface.

The linear geometry of the active region of the Fabry-Pérot devices allows for standing

waves to form between the two facets of the laser, which correspond directly to the cleaved waveguide. By making one of the facets highly reflective, the emission point of the laser is straightforward to define. Furthermore, the linear cavity supports these standing wave patterns, which lead to spatial hole burning. Spatial hole burning along with four-wave mixing are the mechanisms responsible for the multimode operation of Fabry-Pérot lasers [13].

As opposed to Fabry-Pérot devices, the circular geometry of the ring cavities makes unidirectional lasing possible in the absence of facet boundary conditions. Moreover, due to the periodic boundary conditions of the cavity, ring quantum cascade lasers allow for traveling wave solutions. Consequently, the influence of spatial hole burning is reduced in the active region for circular cavities. However, ring quantum cascade lasers still show multimode operation [6].

The realization of circular cavities by employing buried heterostructure waveguides gives rise to another difference. The facet of a ring quantum cascade laser does not correspond to the cleaved edge of the active region but rather to the cleaved InP and air interface. In ring lasers, the outcoupling of the light from the cavity relies on bending losses into the cladding. Then, the mode has to travel through InP before it can reach the actual facet of the device, where it experiences backreflections. The application of an anti-reflection coating at the facet could reduce these reflections.

2.2.1 Spontaneous symmetry breaking in ring quantum cascade lasers

In biased Fabry-Pérot devices, once the lasing threshold is reached, an increase in the current induces the intensity of the laser to also increase, until it reaches rollover. This behavior is shown on panel a) of figure 2.3, for the Fabry-Pérot laser from figure 2.2.

When a ring quantum cascade laser is placed under bias, the geometry allows electromagnetic waves to form in the cavity and propagate in opposite directions. The light-current characteristics of an epitaxial-side down mounted device from the original ring laser design published in [7] are shown on panel b) of figure 2.3.

After the lasing threshold, the ring laser goes through a bidirectional regime, where it emits the same average output power in both lasing directions. In this shaded bidirectional regime on panel b) of figure 2.3, the light-current curve of the laser follows the same path for both directions and looks similar to the light-current curve of a Fabry-Pérot device. The length of the bidirectional regime, and its connection to the operation of the laser will be discussed in section 3.3.

By the further increase of the injection current, a spontaneous symmetry breaking between the two lasing directions is observed. At the symmetry breaking point, the laser chooses its main propagation direction, while the counter-propagating direction experiences a loss. Therefore, when measuring the outcoupled light from the cavity, one has to differentiate between two different cases, as shown in figure figure 2.4.

Following the color coding of panel b) from figure 2.3 and fixing the detector on one side of the laser, when the main mode propagates in the clockwise direction, the light collected onto the detector corresponds to the main propagation direction, as shown in figure 2.4 panel a). However, if the laser is switched on again, a different lasing state can

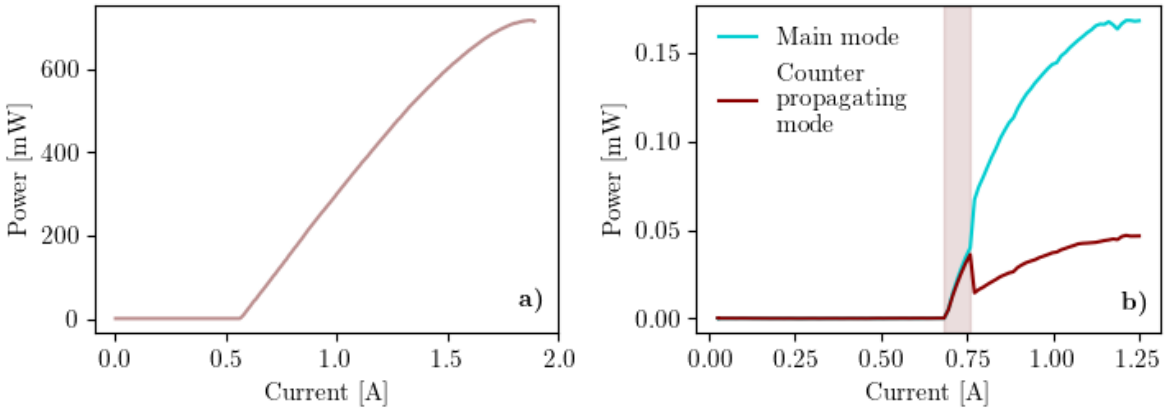

Figure 2.3: Light-current characteristics. Panel a) shows the light-current curve of a Fabry-Pérot quantum cascade laser (EV2017D, 05-ADAL), while panel b) shows the light-current characteristics of a ring quantum cascade laser (EV2394A, Ring12), with a shaded bidirectional regime, followed by a spontaneous symmetry breaking. In ring quantum cascade lasers, the inability to outcouple the light efficiently from the cavity results in low output power compared to Fabry-Pérot devices.

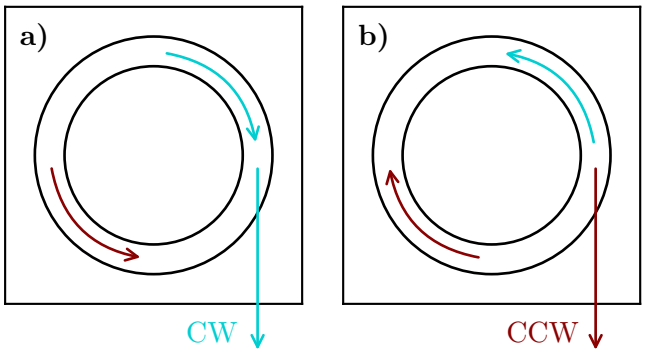

Figure 2.4: Lasing directions of ring quantum cascade lasers. Panel a) depicts the case when inside the cavity, the main mode propagates in the clockwise direction. Measuring perpendicularly to the laser facet, this mode can be collected onto the detector. Panel b) depicts the case when the main propagation direction is counterclockwise, therefore, without moving the detector, the remainder of the counter propagation mode can be captured.

be reached, when the main mode propagates in the counter-clockwise direction. Therefore, without moving the detector, what remains from the counter-propagating direction after the symmetry breaking can be collected.

The occurrence of symmetry breaking is a fundamental feature of ring quantum cascade lasers, which can be theoretically studied by the pair of Maxwell-Bloch differential equations [14, 15].

2.2.2 Coupled modes equations

To study the dynamics of the laser and reproduce the symmetry breaking behavior between the two counter-propagating modes in the cavity, a theoretical model based on a mean-field approach applied to the semiconductor ring lasers [16] is used. The discussion of the coupled modes equations closely follows [15].

The time evolution of the two counter-propagating electric fields $E_{1,2}$ in the cavity is studied, which contributes to saturating the gain n in a ring cavity, using the following dimensionless equations:

$$\begin{aligned} \frac{dE_{1,2}}{dt} &= (1+i\alpha)[\xi_{1,2}n - 1]E_{1,2} - (k_d + ik_c)E_{2,1} \\ \frac{dn}{dt} &= 2\gamma[\mu - n(1 + \xi_1|E_1|^2 + \xi_2|E_2|^2)], \end{aligned} \tag{2.1}$$

where the gain saturation is given by

$$\xi_{1,2} = 1 - s|E_{1,2}|^2 - c|E_{2,1}|^2, \tag{2.2}$$

with normalized self- and cross-gain saturation coefficients, s and c respectively. For symmetry breaking to happen, the gain saturation coefficient has to satisfy the condition $s = \frac{c}{2}$ [14].

In this model, the two counter-propagating field modes are coupled through the conservative and dissipative scattering coefficients, k_c and k_d. Furthermore, α corresponds to the dynamical linewidth enhancement factor, which accounts for the phase-amplitude coupling.

The pumping parameter μ also needs to be taken into account, which is normalized to the threshold current, hence equals to 1 at the lasing threshold. Additionally, $\gamma = \frac{\tau_p}{\tau_s}$ gives the ratio between the photon lifetime and the scattering time.

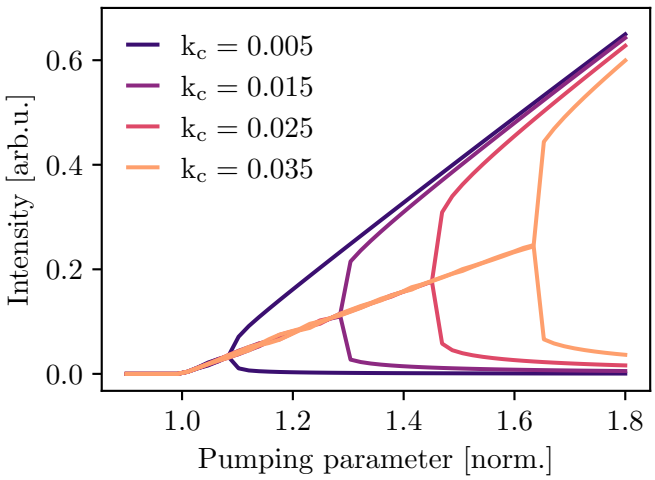

Figure 2.5: Symmetry breaking as a function of the normalized pumping parameter for different values of the conservative coupling parameter between the two counter-propagating modes in the active region of a ring quantum cascade laser.

By implementing (2.1) and using the values given in [15], namely $\alpha = 0.5$, which was estimated from Fabry-Pérot devices, fabricated from the same heterostructure, and $s = 2$, estimated from pulsed light-current measurements, symmetry breaking between the two counter-propagating modes can be simulated. For simplicity, since the dissipative coupling between the two-counter propagating modes is small [16], k_d is neglected, and the time-averaged intensity as a function of the normalized pumping parameter for different values of k_c is calculated.

As figure 2.5 shows, the position of the symmetry breaking point is related to the amount of backscattering present in the cavity. Since the threshold for unidirectional lasing increases with increasing k_c values, to reach unidirectional operation in ring lasers, it is necessary to reduce the backscattering.

Furthermore, from the (2.1) the time evolution of the electric fields in the bidirectional regime can be extracted as well, by starting from random noise. As shown on figure 2.6 for a low conservative backscattering parameter $k_c = 0.01$, a periodic energy exchange between the two directions is observed. This means, that the two counter-propagating directions are not always identical in the bidirectional regime, and in measurements, we only see their averaged value.

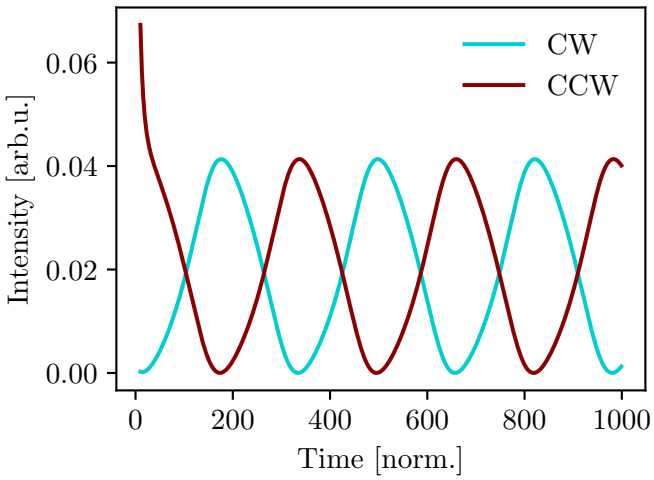

Figure 2.6: Time evolution of the electric field in the bidirectional regime based on the coupled mode equations reveals a periodic energy exchange between the two counter-propagating directions.

2.2.3 Spectrum of ring quantum cascade lasers

The Risken-Nummedal-Graham-Haken (RNGH) instability predicts the appearance of multimode instabilities of ring lasers with a fast gain medium and unidirectional lasing, but only on high pumping rates, at least nine times above the lasing threshold current [17, 18]. The mode proliferation is attributed to the oscillation of the population inversion at the Rabi frequency at high pumping rates, which then modulates the gain of the laser, resulting in side modes separated by approximately the Rabi frequency.

Due to the short upper-state lifetime of quantum cascade lasers, the possibility of observing an RNGH multimode instability is predicted [19]. The ring quantum cascade laser is similar to the original system studied for RNGH instability, but shows a low threshold of the multimode operation. This violation of the RNGH instability leads to a conclusion that additional factors, such as the finite linewidth enhancement factor, and dispersion of the cavity could also contribute to inducing multimode instabilities [6], furthermore a possible built-in saturable absorption in the cavity, resulting from the Kerr lensing effect, is also discussed in the literature [13].

Optical Frequency Combs

The atomic-like nature of the intersubband transitions, meaning transparency on both sides of the transition energy, and the unipolarity of the quantum cascade lasers enable the design and realization of broadband emitters [20]. This feature is beneficial because broadband quantum cascade lasers show operation as optical frequency combs [20, 21], which makes them attractive for spectroscopic applications. Optical frequency combs, first demonstrated in mode-locked lasers [22], are coherent radiations, generated by an optical source, with a spectrum that consists of a set of equally spaced spectral modes, like a ruler in the frequency domain. The spectral lines have a well-defined phase relationship and can be found at frequencies f_n given by

$$f_n = n f_{rep} + f_{ceo}, \tag{2.3}$$

where the spectral lines are spaced at multiple integer values n of the repetition rate f_{rep} of the laser away from each other. Additionally, the first spectral line of the frequency comb is shifted by the carrier-envelope offset frequency f_{ceo}.

Such a frequency comb is schematically illustrated in figure 2.7.

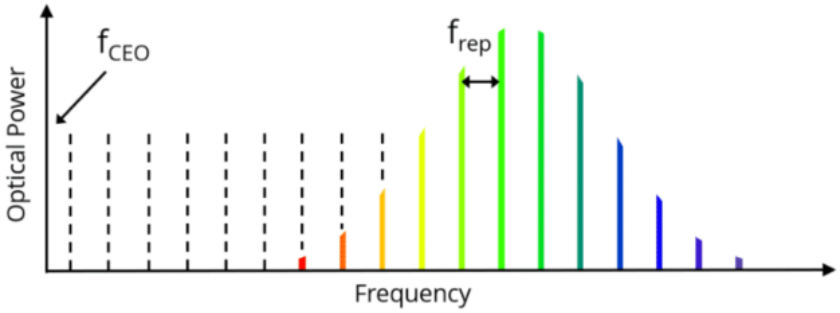

Figure 2.7: Schematic drawing of a frequency comb, with equally spaced discrete spectral lines. The figure is reprinted from [23]

The onset of multimode operation in quantum cascade lasers is triggered by nonlinear effects [13]. Namely, in the case of Fabry-Pérot devices, spatial hole burning and four-wave mixing generated by Kerr-nonlinearity are responsible for establishing the stable phase relationship and inducing mode proliferation [19, 20].

The materials used for quantum cascade lasers, III-V semiconductors, are characterized by huge nonlinearities, which makes them prone to experience multimode instabilities. On top of that, as shown earlier for mode-locked lasers [24], and in optical microresonators

[25], ring cavities enable the spontaneous formation of dissipative Kerr solitons, which was demonstrated experimentally in quantum cascade lasers [7]. Dissipative Kerr solitons are self-organized optical waves preserving their waveform ($sech^2$) when propagating in dispersive media by balancing the effect of the media with the Kerr nonlinearity of the laser.

The conditions of soliton generation are sufficiently small optical backscattering, which allows unidirectional lasing, and a ring cavity with anomalous group velocity dispersion to ensure the balance for the Kerr effect [7].

2.3 Transfer matrix formalism

Ring quantum cascade lasers suffer from low output powers. To enhance their performance, and as an attempt to control the spontaneous symmetry breaking, anti-reflection coatings are going to be applied on their facets to lower the reflections at the InP and air interface.

To design dielectric coatings for quantum cascade lasers, the transfer matrix formalism [26] can be used, which describes the propagation of electromagnetic waves in layered media. The description of the theory used closely follows [27].

As mentioned earlier, when we measure the outcoupled light from a ring cavity, the most intensity contribution comes from the light that propagates perpendicularly to the facet, therefore, in this treatment, only the normal incidence of electromagnetic waves on dielectric material layers are considered.

A monochromatic plane wave with amplitude E_{in} propagating perpendicularly towards a planar interface between two dielectric materials will be reflected and refracted from the boundary, as shown in figure 2.8, where the wave leaves media 1 with refractive index n_1 and enters media 2 with n_2.

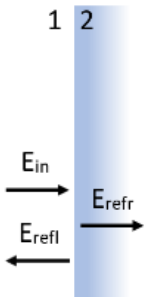

Figure 2.8: The incident electric field gets reflected, as well as refracted from the boundary of two dielectric layers. The figure is reprinted from [27].

Therefore, the amplitudes of the reflected E_{refl} and refracted E_{refr} electric fields in the two media can be written using the Fresnel formulas, where they are compared to the incident electric field as

$$\begin{aligned} E_{refr} &= t_{12} E_{in} \\ E_{refl} &= r_{12} E_{in}, \end{aligned} \tag{2.4}$$

with the proportionality factors t_{12} and r_{12} being the Fresnel coefficients. The Fresnel coefficients are dependent on the refractive index of the media as

$$\begin{aligned} r_{12} &= \frac{n_1 - n_2}{n_1 + n_2} \\ t_{12} &= 1 + r_{12}. \end{aligned} \tag{2.5}$$

From equations (2.5), the reflectance R_{12} and transmittance T_{12} can be calculated in the following way

$$\begin{aligned} R_{12} &= |r_{12}|^2 \\ T_{12} &= \frac{n_2}{n_1}|t_{12}|^2. \end{aligned} \tag{2.6}$$

The extension of the one interface system into a layered media, with multiple dielectric boundaries, is shown schematically in figure 2.9. This treatment is needed in the design of dielectric coatings because, sometimes, multiple thin layers of dielectric materials are stacked to achieve the desired reflectance and transmittance of the system.

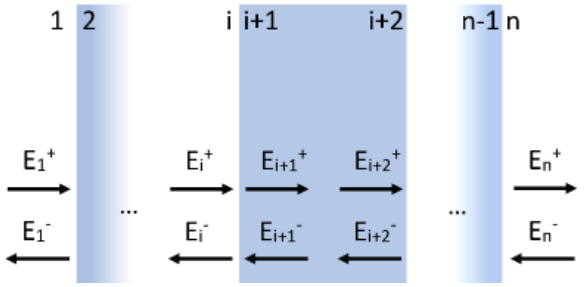

Figure 2.9: Layered media with multiple dielectric interfaces where the electromagnetic waves get reflected and refracted. The figure is reprinted from [27].

To treat the total reflection and refraction of the electric field while propagating through a layered media, at each interface, the amplitude of the electric field is divided into a right E_i^+ and left propagating component E_i^-. For these amplitudes, the matrix equation at every dielectric boundary can be written as

$$\begin{bmatrix} E_{i+1}^+ \\ E_i^- \end{bmatrix} = \begin{bmatrix} t_{i,i+1} & r_{i,i+1} \\ r_{i,i+1} & t_{i,i+1} \end{bmatrix} \begin{bmatrix} E_i^+ \\ E_{i+1}^- \end{bmatrix}, \tag{2.7}$$

with the scattering matrix.

In a similar manner, the reflections and refractions can be expressed with the help of a propagation matrix at the interfaces by

$$\begin{bmatrix} E_{j+1}^+ \\ E_{j+1}^- \end{bmatrix} = \begin{bmatrix} e^{-ikd_{j,j+1}} & 0 \\ 0 & e^{ikd_{j,j+1}} \end{bmatrix} \begin{bmatrix} E_j^+ \\ E_j^- \end{bmatrix}, \tag{2.8}$$

with $d_{j,j+1}$ being the distance between two interfaces, and k the wavenumber.

It is important to note, that the scattering and propagation matrices can be transformed into each other. In the description of a multi-layered system, propagation matrices $P_{i,i+1}$ are applied in the following way to relate the electric field amplitudes of all the layers

$$\begin{bmatrix} E_n^+ \\ E_n^- \end{bmatrix} = \prod_{i=1}^{n-1} P_{i,i+1} \begin{bmatrix} e^{-ikd_{j,j+1}} & 0 \\ 0 & e^{ikd_{j,j+1}} \end{bmatrix} \begin{bmatrix} E_i^+ \\ E_i^- \end{bmatrix}. \tag{2.9}$$

Then, to extract the Fresnel coefficients of the system and calculate the total reflectance and transmittance, the propagation matrix has to be transformed into the scattering matrix.

The above-described method can be used to optimize the thicknesses and materials used through their refractive index to create dielectric coatings. For example, in the case of anti-reflection coating, one wants to increase the transmittance of the facet by applying thin dielectric layers.

2.4 Measurement techniques

In this section, the basic electrical, optical, and spectral characterization techniques of quantum cascade lasers are discussed. From the light-current-voltage characteristics, described in subsection 2.4.1, the threshold current density and slope efficiency of quantum cascade lasers can be extracted. The emission spectrum of the laser devices can be recorded using Fourier Transform Infrared Spectrometers (FTIR), discussed shortly in subsection 2.4.2.

2.4.1 Measurement of the light-current-voltage (LIV) characteristics

Usually, the characterization of laser devices starts with recording the LIV curves of the quantum cascade laser, first in pulsed operation on a low duty cycle with short electrical pulses. This is to prevent the overheating of the device. Then, the measurements are repeated, and by slowly increasing the duty cycle, the lasing threshold changes when approaching the continuous wave operation. Monitoring the change in the threshold current density while increasing the duty cycle helps to determine the efficiency of heat dissipation in the device.

Once the continuous wave operation is reached at a low temperature, typically at -20°C, the measurement is repeated at various temperatures as well. By doing so, device properties such as the threshold current density, dynamical range, slope efficiency, and rollover can be extracted.

The IV characteristics, shown on the left side of figure 2.10, can be extracted by recording the voltage of the device as a function of the changing bias. The Shockley equation dictates the diode behavior of quantum cascade lasers, and the kink that appears is attributed to the photon-assisted transport. However, recording the IV to observe symmetry breaking is not enough, because it looks the same in both directions. Therefore optical characterization of the laser devices is also needed. Since ring quantum cascade lasers have low output powers, to measure the intensity, a more sensitive detection is used, than a power meter.

Such an LI curve, as shown on the right side of figure 2.10 results from collecting the outcoupled light from the cavity onto a cooled Mercury Cadmium Telluride (MCT)

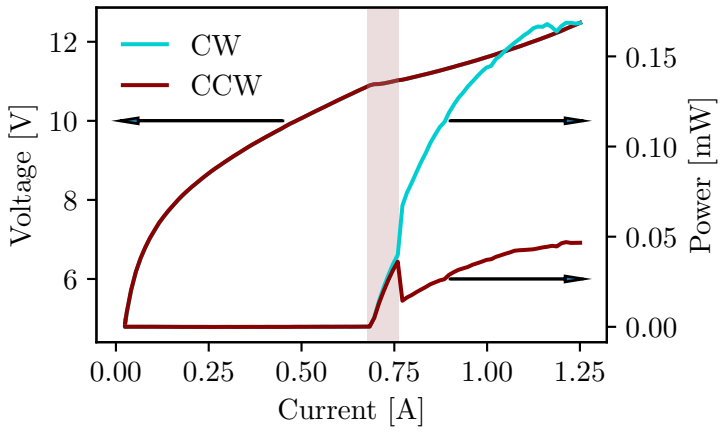

Figure 2.10: LIV curves of the main and counter-propagating modes of a ring quantum cascade laser from the original design published in [7]. The IV characteristics are similar for both directions, but in the LI measurements, symmetry breaking can be observed.

detector. As part of this thesis work, the MCT detector used for the LI measurement was calibrated, with an estimation of the responsivity of 930 V/W. Since the outcoupled light from the cavity is a diverging wave, a focusing lens must be placed before the detector to collect the light. The clockwise (CW) and counter-clockwise (CCW) lasing directions, visualized in figure 2.4, are measured by switching the laser on and off until the preferential direction in the cavity changes.

LIV characteristics for ring lasers, along with providing the threshold currents and slope efficiencies, also let us measure the length of the bidirectional regime, which is directly related to the backscattering in the cavity.

2.4.2 Recording of the spectral data

To measure the spectrum of ring quantum cascade lasers, a Fourier Transform Infrared Spectrometer (FTIR) is used, which is a well-established spectroscopic technique based on the Michelson interferometer. A simplified setup consists of a source (quantum cascade laser in our case), a beam splitter, a fixed and moving mirror, and a detector. Depending on the path difference due to the movement of the mirror, the beams interfere either constructively or destructively with each other. The layout of the elements of the interferometer is shown in figure 2.11.

The detector, most of the times a Deuterated L-alanine-doped TriGlycine Sulfate (DLaTGS) inside the setup, records the interferogram, the first-order autocorrelation function of the electric field, as a function of the delay, the distance moved by the moving mirror. To get the intensity spectrum, the Wiener–Khintchine theorem is used, which states that the Fourier transform of the first-order autocorrelation function gives the power spectrum [29].

For the spectral measurements of ring lasers, mainly the rapid scan mode of FTIR is used, either with a cooled MCT, which provides higher resolution and better signal-to-noise ratio, or a DLaTGS detector, which can operate at room temperature, therefore it

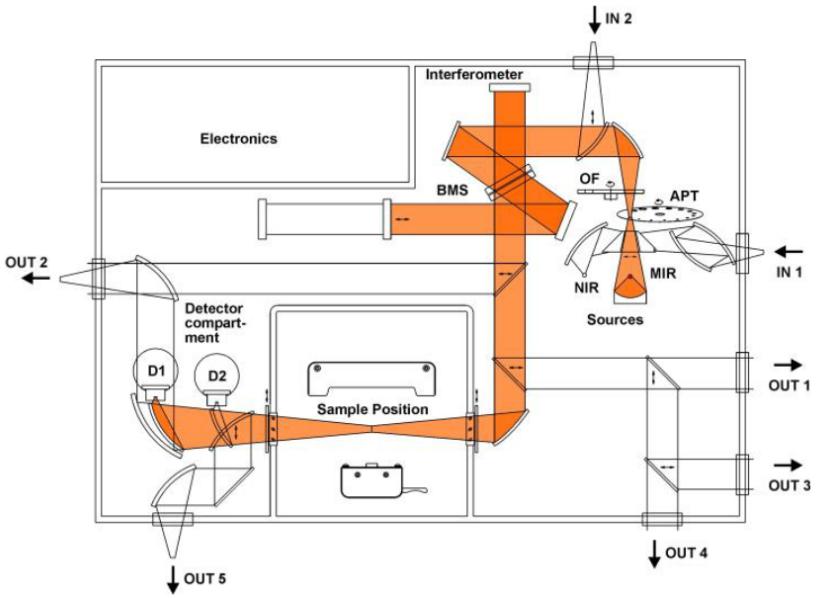

Figure 2.11: Layout of a Fourier Transform Infrared Spectrometer (Bruker Vertex 80/80V). The figure is reprinted from [28]

is more convenient to use. Additionally, it provides better linearity, which is suitable for higher-power devices.

In figure 2.12, the corresponding intensity spectra over the dynamical range of the laser devices from figure 2.10 are shown, with regions of single and multimode operation.

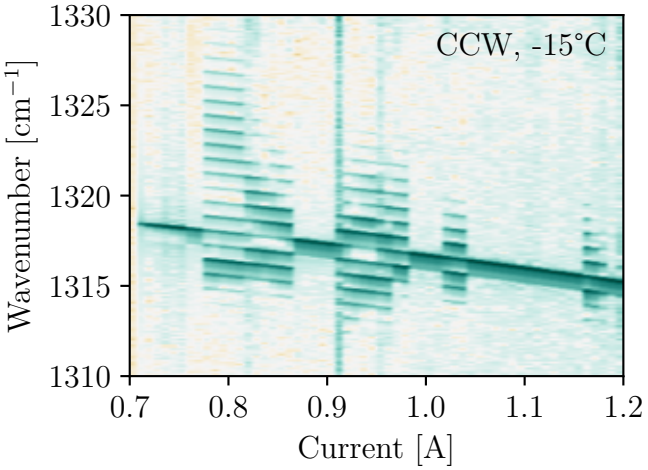

Figure 2.12: Spectral map of laser from figure 2.10 on -15°C shows regions of single and multimode operation

2.4.3 Transmission measurement

FTIRs are used to measure the optical transmittance of materials as well. To study the transmission of the dielectric coatings realized on the laser facets, Fe-doped InP pieces are coated alongside. The dielectric coatings are realized using an electron beam evaporation technique. These coated pieces can be placed in the sample compartment of the FTIR (Bruker Vertex IFS66), where a beam with a broad spectrum goes through the sample. Then the transmitted light can be recorded using an MCT detector, for higher resolution.

Three measurements are performed to characterize coatings: a background scan with an empty sample compartment, transmission measurement through the uncoated substrate, and transmission measurement through the coated Fe-doped InP sample. Then, from these measurements, the transmittance of the dielectric coating can be calculated [30].

Chapter 3

Measurements and Results

3.1 Temperature dependence

Starting with the thermal characterization, the performance of the active regions and the influence of the mounting techniques on the thermal behavior of the lasers used within this thesis will be discussed in section 3.1.

3.1.1 Characteristic temperature

Due to their intersubband design, the threshold current density J_{th} of quantum cascade lasers is only weakly dependent on the temperature [10]. The shift of the lasing onset to higher values with increasing temperature T can be expressed as

$$J_{th}(T) = J_0 e^{\frac{T}{T_0}}, \tag{3.1}$$

where T_0 corresponds to the characteristic temperature of the device, which is associated with the temperature dependence of the threshold current density. Larger values of T_0 mean that J_{th} increases more slowly with rising temperatures. Therefore, for stable laser operation over a wide range of temperatures, large T_0 is desired.

To determine T_0, one typically measures the LIV characteristics of the devices at various temperatures with short electrical pulses to avoid the heating of the active region. In this way, its temperature can be approximated by the temperature of the submounts, which is easier to measure. Then, by extracting the threshold current densities J_{th} and fitting them exponentially with equation (3.1), the characteristic temperature of the device can be calculated.

To get J_{th}, one needs to divide the measured injection current at the lasing threshold I_{th} by the cross-sectional area of the laser, where the current flows through. J_{th} corresponds to the minimal current density required for the laser to start emitting coherent radiation.

For this characterization, we chose two laser devices of size seven from the egg shape design, which will be discussed in section 3.2. Each is fabricated from a different heterostructure. The layer EV2017 is based on a strained design with 45 periods, while EV2041 is a lattice-matched layer with 50 periods. They are single-stacked designs and lase on similar wavelengths, around 8 µm .

We measured the devices in pulsed mode, with 1% duty cycle electrical pulses on temperatures ranging from -20°C to 60°C. The optical output was focused on a cooled MCT detector and acquired with a Lock-In amplification scheme. The resulting LIV measurements are shown on panels a) and b) of figure 3.1. The laser was turned on for each measurement point multiple times, and then the final values were averaged. We can see a different feature of the LI curves, compared to Fabry-Pérot devices, because of the symmetry-breaking behavior, and its averaging shows us the preferential direction of the device at different temperatures. This unique feature will be discussed in more detail in section 3.6.

By fitting the threshold currents with the equation (3.1), as shown on panels c) and d) of figure 3.1, we calculated the characteristic temperatures of the aforementioned layers.

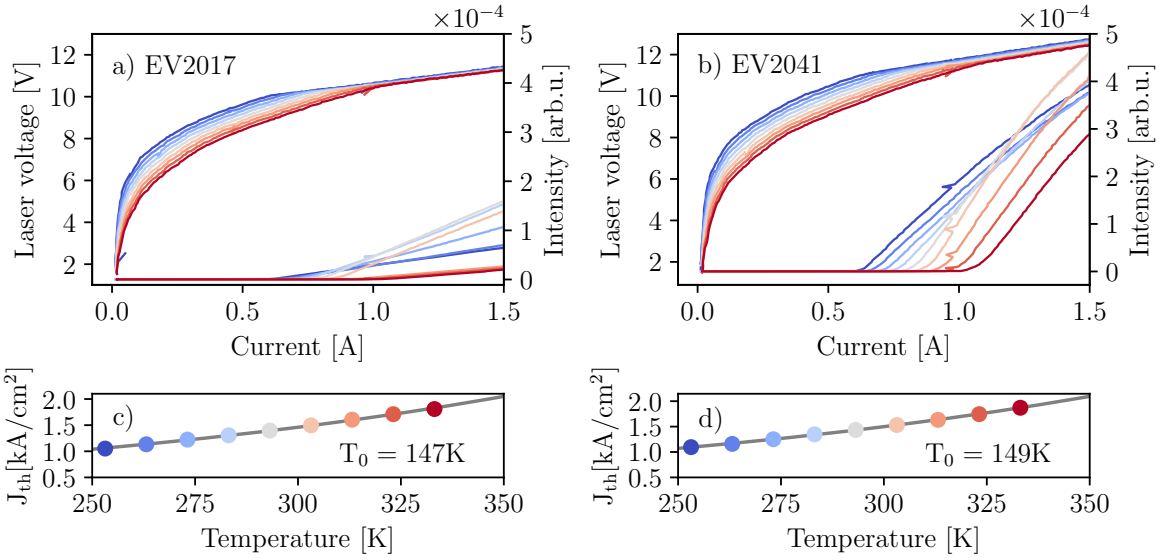

Figure 3.1: LIV measurements and extracted T_0 values of two comparable egg lasers fabricated from different epitaxial layers. Panel a) [b)] shows the temperature-dependent 1% pulsed LIV measurements of the layer EV2017 [EV2041] between -20°C and 60°C. By extracting the threshold current densities at different temperatures and fitting it with equation (3.1) as shown on panel c) [d)] for the layer EV2017 [EV2041], we can calculate $T_0 = 147 \pm 5$K [$T_0 = 149 \pm 5$K]. The colors of the curves in panel a) [b)] correspond to the temperature values of panel c) [d)].

The characteristic temperatures of these devices do not deviate significantly from each other, with values around 147 ± 5K for EV2017 and 149 ± 5K for EV2041. The largest contribution to the error comes from the extraction of the threshold currents, as due to the pulsed measurements, the kink at the threshold is smoothed out. These values for T_0 are in the expected range for quantum cascade lasers reported in [10, 12], and their similarity might arise from a similar design of the active region, a comparable number of periods, and fabrication of both layers within the same processing run.

3.1.2 Thermal resistance

Due to the characteristic short upper-state lifetime of quantum cascade lasers, to reach population inversion, a large amount of power density needs to be dissipated in the active region, typically between 20-50 $\mathrm{kW} \cdot \mathrm{cm}^{-2}$, which leads to the heating of the device [10].

To control the temperature of the laser, and prevent overheating, the lasers are mounted to a heat sink and are actively cooled. Still, due to the large power density applied to the laser, which heats the laser considerably, it is assumed, that with increasing duty cycle, and especially in continuous wave operation, the temperature of the active region $\mathrm{T_{act}}$ will differ significantly from the temperature of the submounts $\mathrm{T_{sub}}$.

In the ideal case, T_{act} is assumed to be proportional to the dissipated electrical power. As a proportionality factor, the thermal resistance $\mathrm{R_{th}}$ is introduced according to

$$T_{act} = T_{sub} + R_{th} U I, \tag{3.2}$$

where U is the corresponding voltage at a chosen operation current I.

Since one usually records T_{sub}, getting an estimate to T_{act} is also of interest. The average temperature of the active region can be calculated by comparing a temperature-dependent value of the laser in pulsed and continuous wave operation, like the threshold current density. The measurements with 1% duty cycle can be assumed not to heat the device significantly, so for these measurements, T_{sub} is treated to be equal to T_{act}.

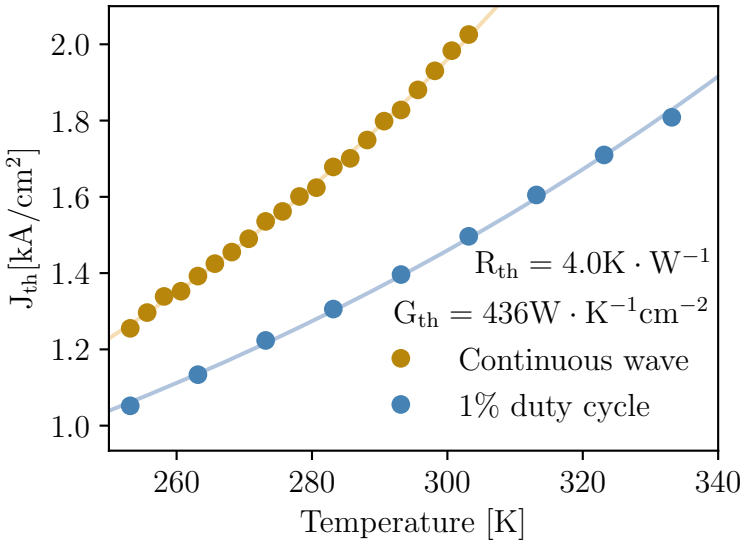

Figure 3.2: Temperature sweep measurements on pulsed and continuous wave operation. Using (3.1) we estimate R_{th} $4.0\frac{K}{W}$. By performing the same calculations, but with J_{th}, we can estimate G_{th} $436\frac{W}{Kcm^2}$

At the lasing threshold I_{th}^{cw} in continuous wave operation, for the considered temperature, where T_{sub} is measured, R_{th} can be expressed as

$$R_{th} = \frac{T_0 ln(\frac{I_{th}^{cw}}{I_0^p}) - T_{sub}}{U_{th} I_{th}^{cw}}. \tag{3.3}$$

Using (3.2) with the value for T_0 that we calculated in subsection 3.1.1 R_{th} can be calculated.

In figure 3.2, we show two temperature sweep measurements of the device from the layer EV2017. One is in continuous wave operation, and the other one is with the 1% duty cycle electrical pulses from figure 3.1. We calculated the average value of R_{th} from the different measurement points of the continuous wave operation temperatures, which equals to $4.0 \pm 0.1 K/W$, and enables the estimation of T_{act}. The calculated thermal conductivity G_{th} of around $436\mathrm{W} \cdot \mathrm{K}^{-1}\mathrm{cm}^{-2}$ is also estimated for the same device. These values are of the order of the thermal resistivity and conductivity reported for buried heterostructure waveguides [12].

The extraction of the thermal conductivity was only performed for one of the two layers. As the heat dissipation is mainly determined by the fabrication and mounting, similar values of G_{th} are expected for EV2041.

3.1.3 Thermal properties of mounting

As discussed in the previous section, efficient heat extraction is crucial for the optimal performance of quantum cascade lasers. The thermal resistance depends on the mounting and soldering process of the device. Since minimal values for R_{th} are desired, we explore how J_{th} changes if we mount similar laser devices, either with the epitaxial layer facing the sub-mount or the epitaxial layer being closer to the surface in the buried heterostructure waveguide design. Due to the reduced distance of the active region from the heat sink, improved heat dissipation is expected for epitaxial-side down mounting [10].

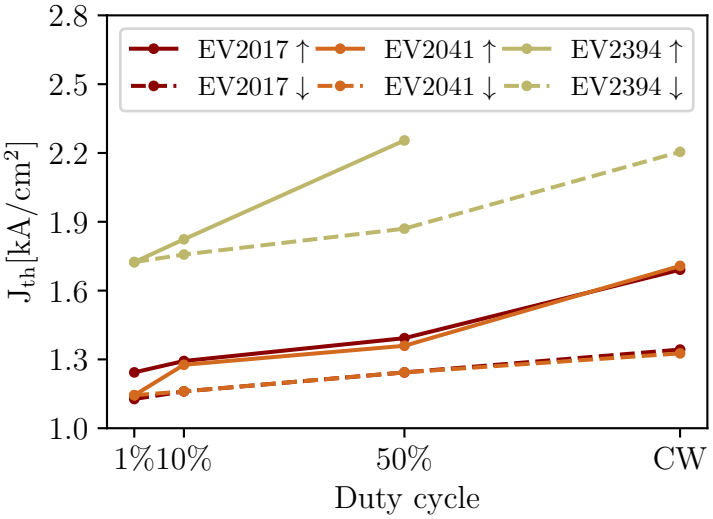

Figure 3.3: Measurement of epitaxial-side up and down mounted ring lasers with 12µm waveguide width on different duty cycles, and continuous wave operation. For all of the three layers, the epitaxial-side down mounting, with the active region being closer to the submount, provides a more efficient heat transfer, and leads to lower threshold current densities.

To check the dependence of J_{th} in pulsed and continuous wave operation, we mounted

two ring lasers with a waveguide width of 12µm from three different processes in the two aforementioned mounting configurations.

We performed the measurements at -20°C, whose results are shown in figure 3.3. Two main features within this data imply the expected improvement of the heat dissipation for the epitaxial-side down mounted lasers. Firstly, at a given duty cycle, we measure lower threshold current densities in the case of lasers mounted epitaxial-side down, signifying lower active region temperatures. Secondly, the threshold current densities of such devices react less sensitively to increasing duty cycles.

By mounting epitaxial-side down, the threshold current density in the case of the layer EV2017 is reduced by 10% in pulsed operation, with 1% duty cycle electrical pulses, and by 20% in the continuous wave operation.

Even though epitaxial-side down mounting shows better thermal properties, it is not always the best choice, as it does not allow, for example, efficient radiofrequency injection. Furthermore, this mounting technique requires smooth top contacts. This strict requirement excludes many functioning lasers and thus lowers the effective processing yield.

3.2 Optimized ring laser design

The ring quantum cascade laser provides a uniform emission of light throughout the whole active region due to the constant bending losses. Since the outcoupling of the mode from the active region is based on bending losses and scattering in the case of lasers with circular cavities, by altering the geometry of the active region and engineering it such that the emission of the light can be spatially focused, the output power can be increased. To achieve this, the Hügelschäffer egg [31] parametrization was used, which allows for optimization of the curvature of the egg shape. Also, by varying the circumference of the lasers, the roundtrip time of the device can be modified as well.

These egg quantum cascade lasers were designed and fabricated by I. H. [32], using the inverted buried heterostructure waveguide process with nominal waveguide widths of 10, 12 and 14 µm, and egg sizes varying from a circumference of 3770 µm for the ring laser, labeled as egg zero in figure 3.4 to 7147 µm for the egg size seven laser, with a lower repetition rate of 12.5 GHz.

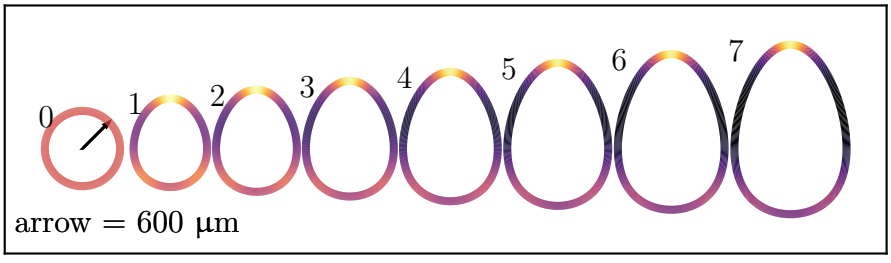

Figure 3.4: Modified circular cavity design based on the Hügelschäffer egg. The colors correspond to bending losses, starting from an equally distributed emission for a ring laser (egg 0) to a more spatially concentrated emission around the tip of egg-shaped devices.

In figure 3.4, the color scale of the laser shapes for the eight different sizes depicts the curvature, with higher bending loss at the tip and lower all around the laser. Due to the exponential dependence of the bending losses on the curvature, the higher curvature at the tip of the egg allows for more light to be outcoupled from the cavity. Going from the ring design, or egg zero, with a uniform curvature and complete rotation symmetry, to egg lasers with larger circumferences, first, as shown on the panel a) of figure 3.5, the distribution of the curvature changes, which leads to a spatially focused bending loss at the tip of the laser, as shown on the panel b) of figure 3.5. Then, the further increase of the circumference of the laser leads to longer roundtrip times at the expense of a small decrease in the bending losses. Despite the loss in output power for the larger eggs due to technical purposes, it is worth using the eggs with the slower repetition rates, as, for example, the radio-frequency equipment is more mature and affordable for lower frequencies.

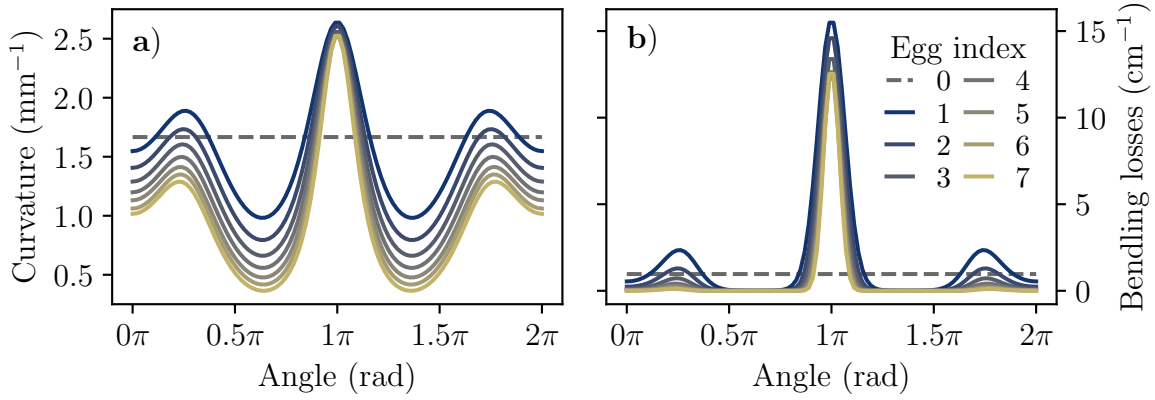

Figure 3.5: Curvature and bending losses of the egg design of different sizes corresponding to figure 3.4 as a function of the angle. On panel a) the engineered curvature, and on panel b) the computed bending losses with a high loss focused at the tip compared to the other parts of the cavity are shown. First, going from an isotropic loss in the case of egg zero to egg one, where the emission is more focused on the tip of the egg. The further increase of the circumference of the laser leads to a slight decrease in the output power of the largest egg lasers.

To confirm the design features of the egg lasers experimentally and compare the different egg sizes, we conducted LI measurements of devices from the layer EV2017 with the same nominal waveguide width of 10 µm in continuous wave operation, at -20°C. Then, we compare the threshold current densities and slope efficiencies of these devices. Unfortunately, egg sizes four, five, and six are not part of the analysis because of a lack of available devices of this design with the given waveguide width.

Based on panel b) from figure 3.5, it is expected when going from egg zero to egg one, the output power to increase significantly, and as the circumference of the laser is further increased, the emission power decreases slightly.

In figure 3.6, we compare the measurement values to the calculations. We can get the total losses α_{tot} from the bending losses, which account for the waveguide losses from free carrier absorption and surface roughness scattering. Furthermore, the tip losses α_{tip} refer

to the bending losses within a ±10° angle around the tip, which we expect to collect when measuring. The ratio of $\alpha_{tot}/\alpha_{tip}$ is expected to be proportional to the slope efficiency of the devices, confirmed by the almost linear dependence of the y scale on panel a) to the x scale. While α_{tot} is proportional to the threshold current density.

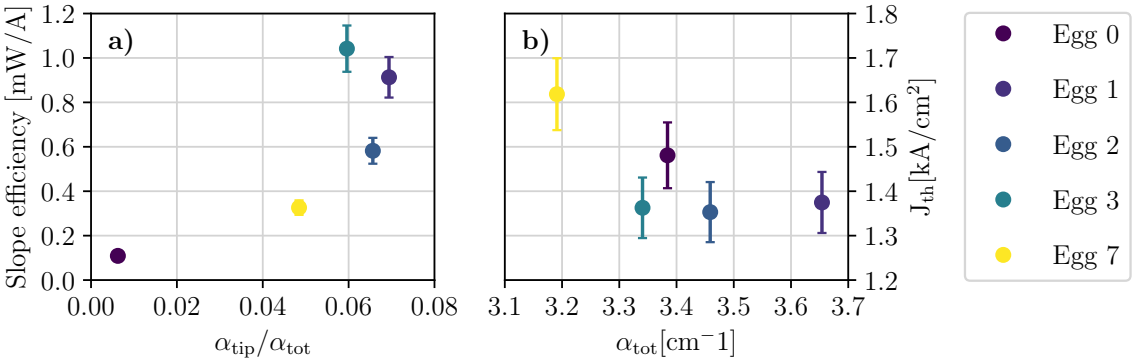

Figure 3.6: Panel a) shows the extracted slope efficiencies from measurements as a function of the calculated ratio of "waveguide and mirror losses". threshold current density as a function of the slope efficiency of different egg sizes.

In figure 3.6, the threshold current densities of the different lasers fall to similar values, which is expected considering we mounted lasers fabricated from the same layer. The error in the measurements can be attributed to various parameters, like the error of the current source, temperature deviation, inconsistencies in the waveguide width, losses due to defects, and due to uncertainty in the fitting regions for the threshold currents and slope efficiencies.

3.3 Relation of symmetry breaking to the backscattering

This section is based on the work of L. Seitner et al. [8].

Due to the RNGH instability, it was not expected that multimode operation in ring quantum cascade lasers is possible on low pumping currents. However, in [6], a multimode spectrum was observed on currents close to the lasing threshold. Furthermore, even stable frequency combs, solitons were recorded in such lasers, both in the mid-infrared [7, 33], and terahertz regimes [34]. In the literature, the appearance of combs in ring cavities has been attributed to phase turbulence [35, 36], furthermore, defects in the cavity were found to cause multimode operation as well[37].

Using the Maxwell-Bloch model [38], it is shown that for the multimode operation of ring quantum cascade lasers, a finite coupling between the main mode and the weaker counter-propagating mode is necessary. The counter-propagating mode can be thought of as a consequence of the distributed backscattering in the cavity [8], which can be due to any defects in the laser. For example, on panel a) of figure 3.7, a cross-section of the original ring process of [7] shows some growth defects, visible as dark areas right next to and above the active region, in comparison with a defect-free fabrication on panel b).

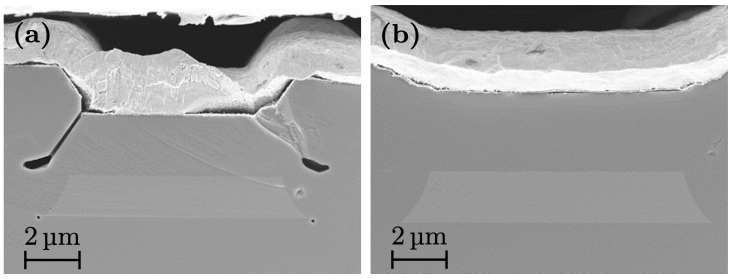

Figure 3.7: Scanning electron microscope images of cross sections of the buried heterostructure waveguides of two ring lasers from two different fabrication processes. The light trapezoidal shape in the center is the active laser region, which is fully encapsulated by the darker InP cladding. On panel a), a device with defects is visible, while the device shown on panel b) is defect-free. The figure is reprinted from [8].

Numerical simulations based on the coupled modes equations, discussed in subsection 2.2.2, predict that the threshold for the unidirectional lasing increases linearly with the amount of backscattering present in the laser. Therefore, LIV measurements provide an indication for the backscattering, as the length of the bidirectional regime can easily be extracted.

Our measurements are in good agreement with the findings of [8]. In figure 3.8, spectral sweep and LI measurements are shown for devices from the same fabrication runs as figure 3.8. On panel a), multimode operation regimes are observed for a device with defects, hence having a longer bidirectional regime, as shown on the corresponding panel c). At the same time, we measured a purely single-mode emission spectrum, as shown on panel b) for a defect-free device, as indicated by the short bidirectional regime of this laser, as shown on panel d).

Based on the numerical predictions and measurements, a key prerequisite for the formation of dissipative Kerr solitons in ring quantum cascade lasers is unidirectional lasing [7], but also a weak counter-propagating mode that can couple to the main mode [8]. Therefore, the suppression of the backscattering in the cavity is needed to reach the limit of single-mode operation, but still, with a finite amount of backscattering, that maintains the weaker counter-propagating mode. Because, in contrast, a perfect ring cavity shows a complete decay of the counter-propagating mode and leads to single-mode lasing.

The symmetry-breaking point allows for the estimation of the backscattering coefficient, which is proportional to the ratio of the current at the symmetry-breaking point to that at the threshold. In figure 3.9, we show this ratio as a function of the intensity ratios of the main and counter-propagating directions, extracted from various measurements of different egg-shaped devices. It confirms, that for multi-mode operation to happen, a higher backscattering coefficient is needed in the cavity, which simultaneously elongates the bidirectional regime. At the same time, the increased backscattering enables more efficient energy transfer between the two lasing directions, which in turn leads to a decrease in the CW/CCW ratio.

The amount of backscattering can be minimized during the fabrication process by employing buried heterostructure waveguides [12] due to a reduction of the refractive index difference between the active region and the cladding. However, the presence of defects,

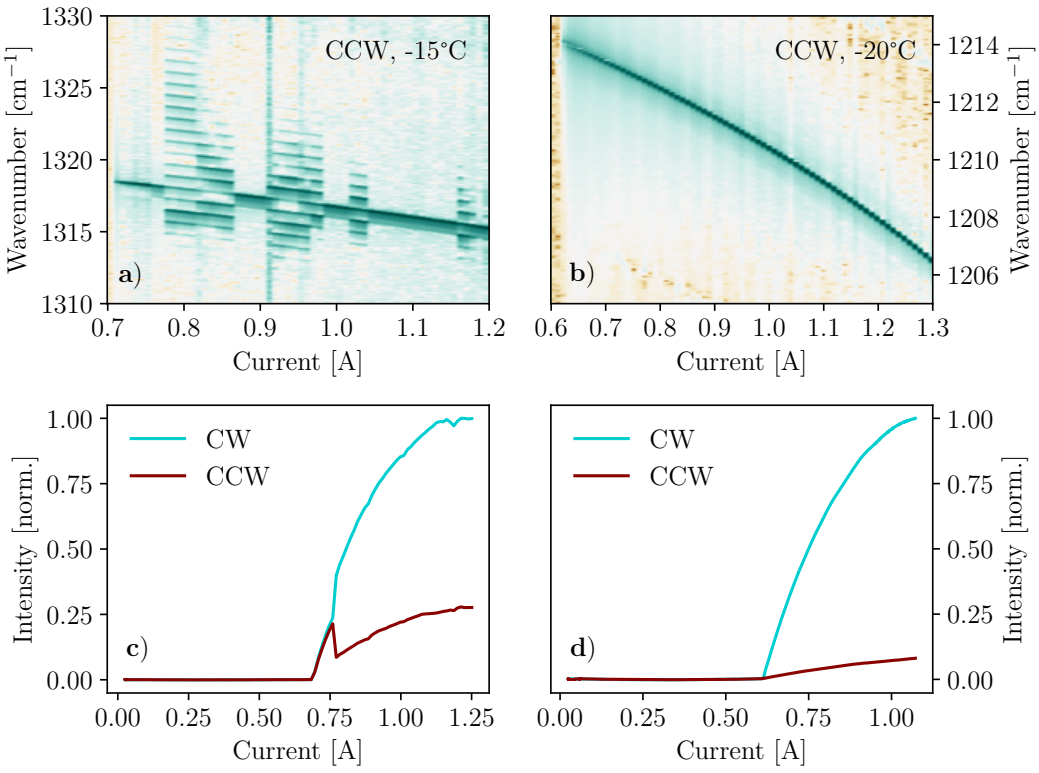

Figure 3.8: Spectral sweep and LI measurements of ring lasers fabricated along with the ones shown on figure 3.7. On panel a), the spectral sweep of the lasing direction CCW is visible, which shows multimode regimes of operation. The LI measurement of this device with defects has a longer bidirectional regime, as shown on panel c). On panel b) the spectral sweep measurement of a defect-free device, corresponding to a similar laser as figure 3.7b) with single line emission is shown, with the corresponding LI measurement on panel d) with a shorter bidirectional regime.

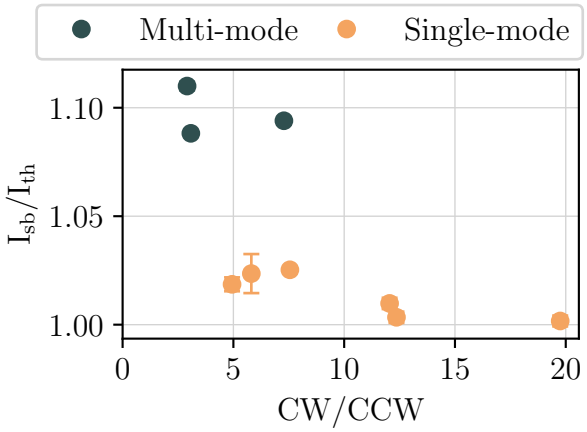

Figure 3.9: The ratio between the threshold for unidirectional operation and the lasing threshold as a function of the intensity ratio between the two counter-propagating modes.

sidewall roughness, and reflections from the laser facet induces conservative backscattering. A fine balance between these contributions is needed for the formation of solitons, however, almost all of them are defined during the growth and fabrication process. The only contribution that is accessible post-process is the reflections from the facets, which will be discussed in section 3.5.

3.4 Spectral identity of modes after symmetry breaking

As discussed in section 3.3, the weaker counter-propagating direction is assumed to be the reflection of the main mode from the different scatterers in the laser. Using the FTIR setup discussed in subsection 2.4.2, we record the spectrum of the emission on two sides of the laser, as depicted in figure 2.4. For these measurements, we use a ring quantum cascade laser from the original design of [7], which shows regions with multimode operation.

Due to the low output power, we use the entrance of the FTIR, which is equipped with a high numerical aperture lens. Then the light is focused onto a DLaTGS detector. Once the lasing threshold is reached, we record the spectrum of the light emitted from one side of the laser, perpendicular to the facet. Then, on the same operation point, we move the laser parallel to its front facet, and without turning it off, we repeat the measurement on the other side. Finally, to confirm the alignment, again, without turning the device off, we go back to the side measured first and remeasure.

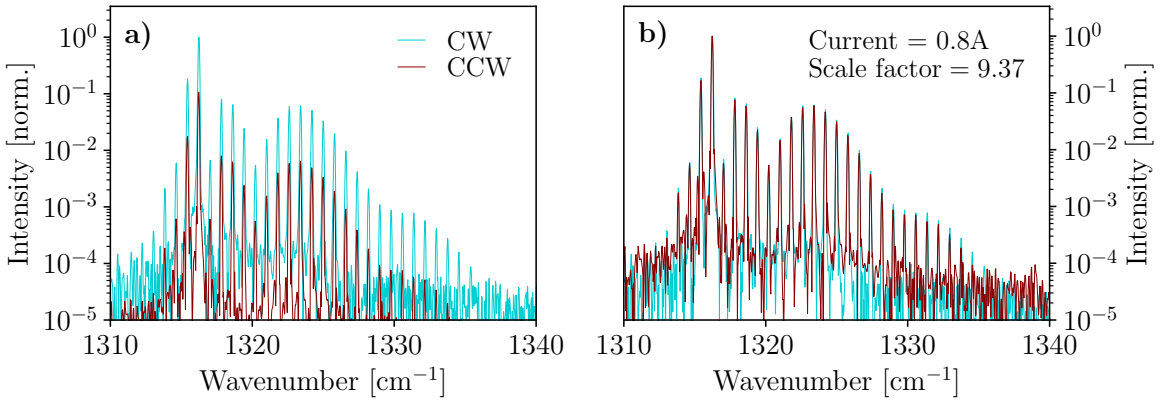

Figure 3.10: Overlapped spectrum of the two counter-propagating modes at the operation point of 0.8A at -20°C. Panel a) shows the obtained spectra from the two sides of the device, without turning it off, plotted on a logarithmic scale. On panel b) the same spectra are visible, but with a rescaled CCW direction by a scaling factor of 9.37 to show their identity.

At the chosen operation point of 0.8A at -20°C, if we overlap the obtained spectra on a logarithmic scale, as shown on the panel a) of figure 3.10, the CW and CCW direction resembles similar-looking spectra. The spectral identity of the two lasing directions can

be confirmed if we scale the CCW direction by a factor of 9.37 as shown on panel b) of figure 3.10.

Since the spectra of the two counter-propagating directions are almost identical, we confirm that the weaker counter-propagating direction is indeed a consequence of the backscattering in the cavity and it thus not spectrally distinct.

3.5 Symmetry breaking measurements, and anti-reflection coatings

For any practical application of quantum cascade lasers with circular cavities, it would be of great importance to be able to consistently choose the lasing direction of the devices after the symmetry-breaking point at different temperatures. In this section, the effect of an anti-reflection coating on the laser facet is discussed, as an attempt to take control over lasing directions.

So far, it has been discussed that backscattering plays an important role in the length of the bidirectional regime. Scatterers are seen as any kind of defects in the laser, from where the light can get back-reflected, for example, sidewall roughness, impurities in the active region, and reflections from the facet. The first two have to be considered unchangeable post-fabrication, as the impurities in the cavity are determined already during the epitaxial growth process, and the sidewall roughnesses are introduced during the processing of the devices. However, the third type of backscattering, namely the reflection from the facet, is accessible in the finished device.

The reduction of this type of backscattering is going to be addressed in this section by an anti-reflection coating, and its effect on the choice of the lasing direction after the lasing threshold is studied.

Statistical symmetry breaking measurements

Since the goal would be to be able to control the choice of the lasing directions in quantum cascade lasers with circular cavities, we need to perform statistical measurements. Within this subsection, both the employed measurement scheme and the data treatment will be introduced. A discussion and interpretation of the experimental results will be included in the following chapters.

Due to the low output power of the ring lasers, the LI measurements are performed using the setup discussed in subsection 2.4.1 with a nitrogen-cooled MCT detector. At each chosen temperature point, we measure the device 10 times on the same side in order to get a better overview of its symmetry-breaking behavior. In the example dataset shown in figure 3.11, the vast number of LI plots from panel a) are summarised to more easily get an overview of the preferential lasing direction at each temperature point, as shown on panel b). The color scale in these figures corresponds to the operation temperature of the devices. The black columns on panel b) indicate how many times out of the 10 measurements the laser chose the lower output direction at a given temperature, therefore, the remaining colored parts of the columns correspond to the main propagation direction.

Furthermore, two types of measurements are distinguished in our study. In an adiabatic measurement, the injection current is increased slowly above the symmetry breaking

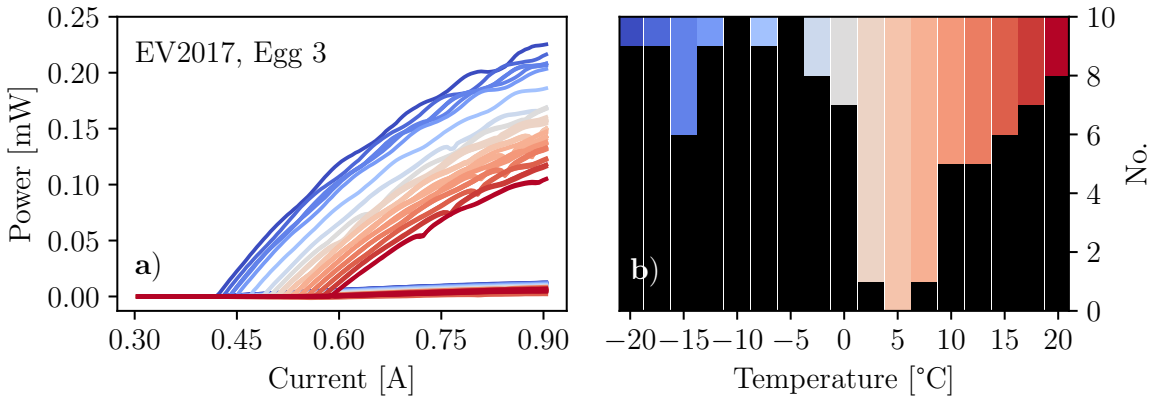

Figure 3.11: Temperature sweep LI measurement of an egg size three laser with 10 repetitions on the same side on temperature points varying from -20°C to 20°C. Panel a) shows all the 10 measurements for each temperature point, while panel b) is extracted from the measurement and visualizes the statistics of the symmetry breaking. At every temperature point marked by the color coding of the horizontal scale, the height of the black column corresponds to the number of measurements when the device chose the weaker counter-propagating direction, while the colored parts of the columns correspond to the measured main preferential direction of the laser.

point, and the data points are recorded as the current is decreased, while in the case of a non-adiabatic measurement, we abruptly turn on the device above the threshold for unidirectional operation. These two types of measurement provide a different behavior of the laser devices, probably due to the different timescale of the thermal dissipation.

3.5.1 Influence of anti-reflection coatings

As mentioned earlier, in ring quantum cascade lasers, due to the shape of buried heterostructure waveguide, there are some limitations in the cleaving. The device is cleaved along the crystalline axes, resulting in a rectangular piece of InP, in which the circular active waveguide is embedded. Consequently, the outcoupled light, as depicted in figure 2.4 gets back-reflected from the InP-air interface, and can potentially get reinjected, contributing then to the counter-propagating mode, or forming a Fabry-Pérot type of cavity between the two facets. Therefore, controlling the reflections from the facet is crucial.

Our approach is to apply an anti-reflection coating for the specific emission wavelength of the device (usually between 7 µm and 9 µm) to reduce the reflections from the facet. We first model the reflectance of the coating applied on the InP cladding, using the transfer matrix formalism discussed in section 2.3. The chosen anti-reflection coating is built up from three layers, 550 nm of Al_2O_3, followed by a layer of 90 nm of Ge and finished with a passivation layer of 10 nm Al_2O_3. The targeted reflectance from the simulated coatings is shown in figure 3.12, with a low reflectance around the wavelengths of interest.

It is expected that the application of such an anti-reflection coating increases the output power of the device, as it decreases the reflectivity of the InP and air interface.

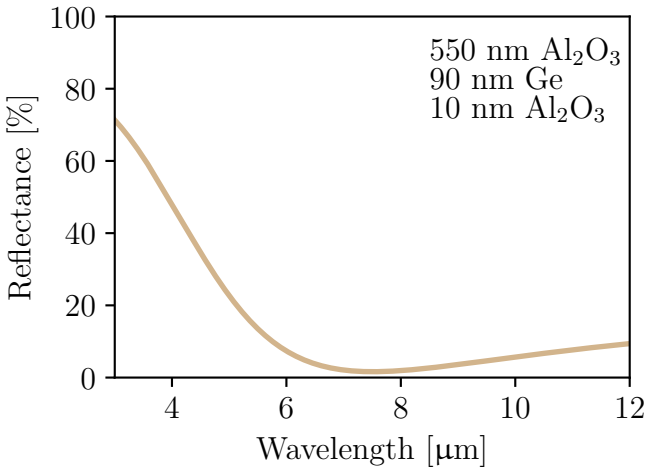

Figure 3.12: Intended AR coating recipe with 550 nm of Al_2O_3, 90 nm of Ge and 10 nm of Al_2O_3 shows low reflectance at around the wavelength 7 nm.

Powermeter measurements of the main mode of an uncoated device, and after the application of the anti-reflection coating confirm, as shown in figure 3.13, that the anti-reflection coating increases the output power. However, uncertainties might arise from the alignment of the laser on the power meter due to the dispersive nature of the outcoupled wave and its low power.

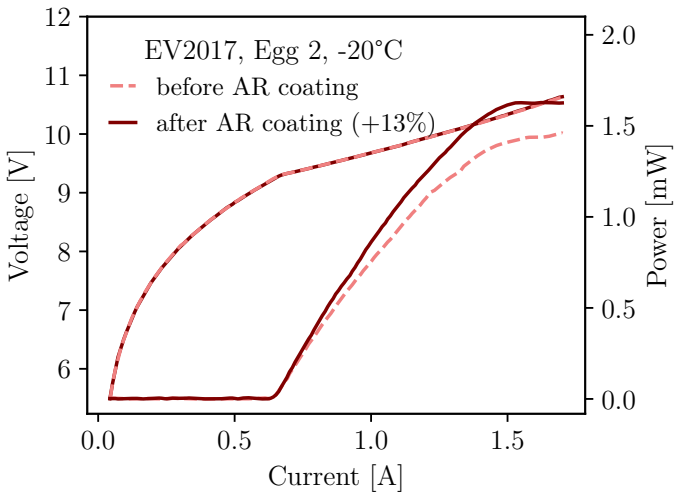

Figure 3.13: The AR coating lets more light to outcouple from the cavity, but it does not change the IV, contrary to Fabry-Pérot devices, where the threshold current density increases.

In the case of these circular quantum cascade lasers, when performing LI measurements, it is unclear whether the light collected on the detector is coming from the main propagation direction only, or whether we collect the mode reflected from the back facet as well. Panel a) of figure 3.14 shows the LI measurements of a device with an anti-

reflection coating on the front facet. When comparing this to measurements of the same device with a highly reflective coating on the back facet, as shown on panel b) of figure 3.14, we enhanced the feedback from the back facet, resulting in a higher output for the counter-propagating direction.

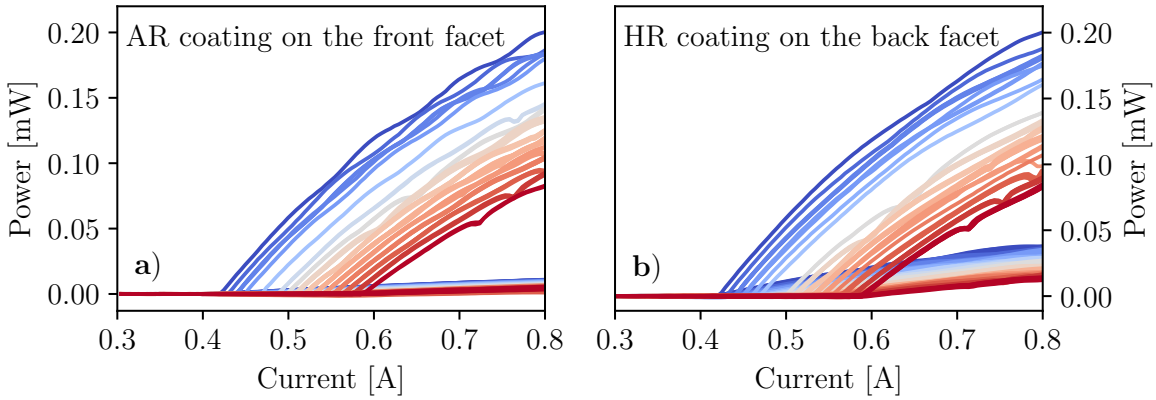

Figure 3.14: LI temperature sweep measurements of an egg size three quantum cascade laser. On panel a), we applied an anti-reflection coating on the front facet of the device, while on the b) panel, the characteristics of the same device with an additional highly reflective coating on the back facet are shown.

Therefore, we can assume, when we are taking LI measurements, that a combination of the two propagation directions is collected onto the detector. In the case of a defect-free fabrication process, indicated by the length of the bidirectional regime, it is fundamentally interesting to investigate the symmetry-breaking behavior further.

Preferential directions of defect-free laser devices

The statistics of the LI measurements of the egg size seven laser from figure 3.14 are shown in figure 3.15. While the measurements in the first row, namely on panels a), b), and c) were performed with an adiabatic current injection, the measurements in the second row, panels d), e), and f) were performed by turning on the laser nonadiabatically at a higher operation point.

When looking at only the adiabatic measurements of the device before any coating, and comparing it to the measurements with the anti-reflective coating on the front facet, we see a slight influence on the lasing behavior as the ratio of operating points with high collected power increases for low temperatures. The additional highly reflective coating at the back facet did not lead to further change.

While turning the laser on non-adiabatically, as shown on panel d), for high temperatures, it completely changed its preferential direction, which could be due to the inefficient thermal extraction when abruptly turning on the laser, especially in the epitaxial-side up mounting configuration. Then, as we can see if we compare panels d) and e) of figure 3.15, the anti-reflection coating influenced the lasing state on positive temperatures. Other than the effect of the highly reflective coating shown on figure 3.14, it does not seem to influence the choice of the lasing directions.

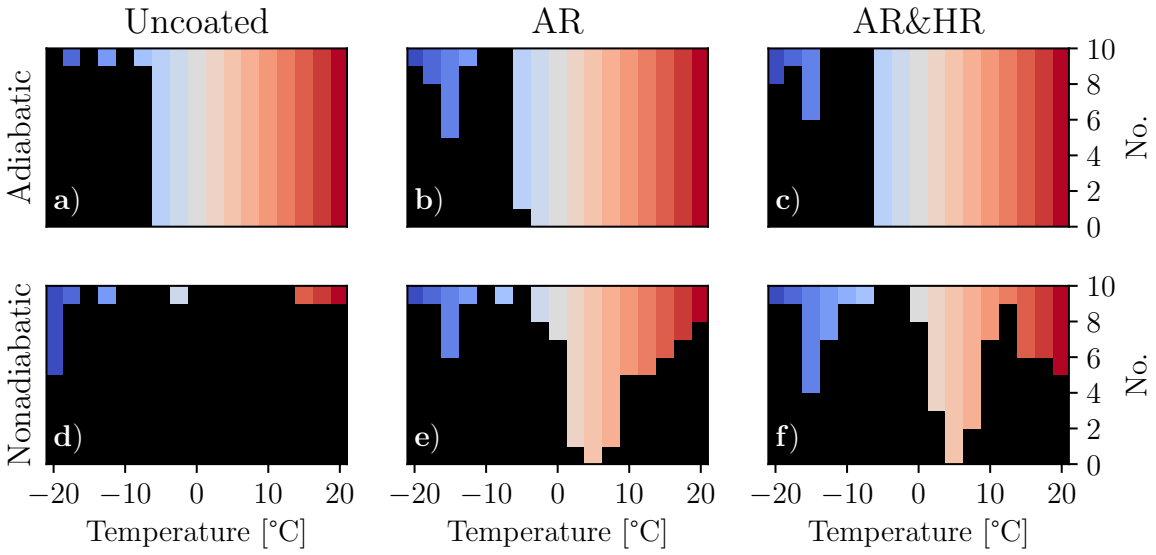

Figure 3.15: Statistics extracted from LI measurements of the same laser device measured on various temperatures between -20°C and 20°C, 10 times at each. Panels a), b), and c) show adiabatic measurements, while in the case of panels d), e), and f), the laser was turned on nonadiabatically. The measurements were conducted on an uncoated device of egg size three (panels a, d), with anti-reflection coating on the front facet (panels b, e), and with a highly reflective coating applied on the back facet (panels c, f). The device exhibits a strong temperature dependence on the preferential lasing direction, which is influenced by facet coatings for non-adiabatic current ramps.

The same type of coatings and measurements were repeated for multiple devices, and we found that the AR coatings mostly had an influence when the laser had a high output power. In figure 3.16, the symmetry-breaking statistical measurements for the same device from figure 3.13 with a rollover at around 1.5 mW are shown.

From these measurements, similar behavior can be concluded. But in this case, the combination of the anti-reflection coating and the non-adiabatic turning on of the device unlocks access to the higher output power on lower temperature values as well, which would not have been reachable otherwise.

We found that anti-reflection coatings have an effect on the symmetry-breaking phenomena under two conditions. The output power of the lasers needs to be high, and the laser needs to be turned on nonadiabatically.

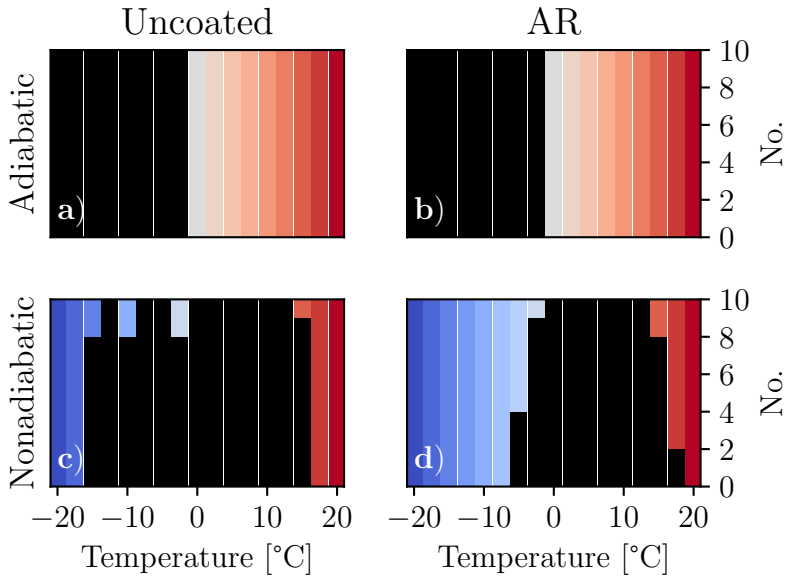

Figure 3.16: Statistics extracted from an egg size two device from the layer EV2017 before anti-reflection coating on panels a) and c) and after anti-reflection coating on panels b) and d) for adiabatic and non-adiabatic measurements. The anti-reflection coating lets us access the main mode at some negative temperatures if the device is turned on non-adiabatically.

3.6 Temperature dependent symmetry breaking

Some of the previously discussed statistical LI measurements show a temperature-dependent symmetry-breaking behavior, meaning that at temperature ranges, the device shows a clear preferential direction. This preference can be so pronounced, that for some devices and temperature set points, the laser would lase in the same direction in all investigated current ramps, as shown in figure 3.17.

This feature of the quantum cascade lasers with circular cavities is not intuitive, as not all the devices show a periodical preferential direction choice with varying temperatures. Seemingly it does not depend on the size of the cavity or the layer used, and it shows up randomly for some of the devices.

To try to reproduce and investigate this temperature characteristic, we introduce a simple analytical model.

Model

We assume that next to the active region, a secondary, passive, low-finesse cavity can be formed between the two cleaved facets, which resemble a Fabry-Pérot resonator. Furthermore, we assume these two cavities to couple to each other.

To build up the model for the aforementioned case, we assume a high-quality factor cavity for the circular waveguide. Its free spectral range (FSR) is given by the equation

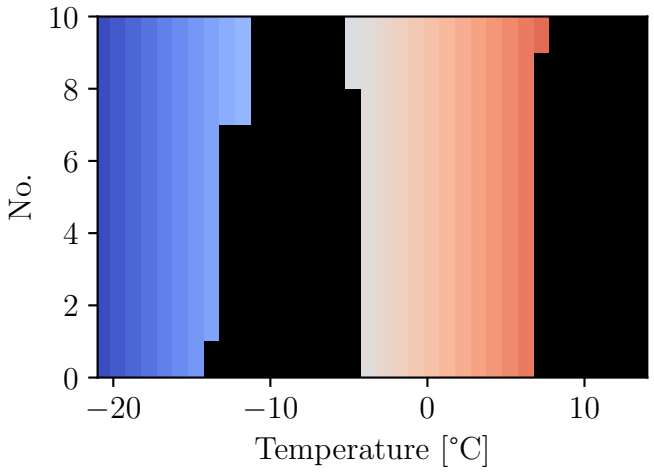

Figure 3.17: Histogram of a laser device of egg size four from the layer EV2041, which was measured 10 times adiabatically at every operation temperature, shows regions with a clear preferential direction.

$$f_{FSR} = \frac{c}{Ln}, \tag{3.4}$$

with n being the effective refractive index of the cavity materials, namely InGaAs and InAlAs. The parameter L corresponds to the circumference of the cavity and c to the speed of light. An example FSR is shown in 3.18 with narrow lines.

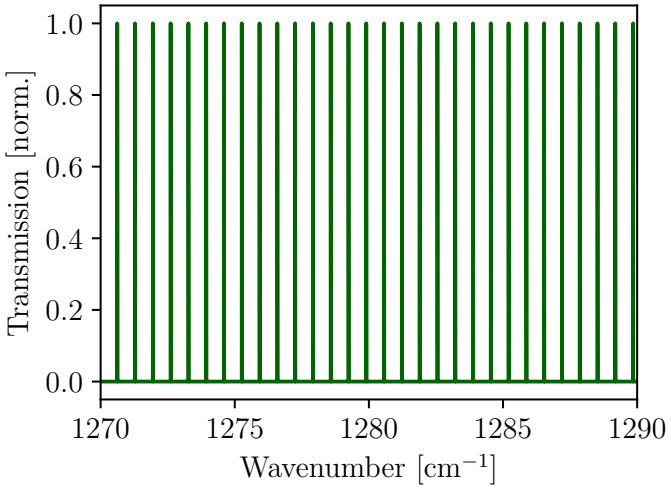

Figure 3.18: Resonances of the circular cavity with an assumed high quality factor.

Due to the buried heterostructure waveguide, the light gets outcoupled from the cavity to the InP cladding. When the emission of the laser is perpendicular to the facet, the light could start to bounce back and forth between the facets, but with high losses. Therefore, we describe this cavity by an extremely low quality factor between the emission point, the

tip of the laser, and the cleaved InP facet of the laser. For this Fabry-Pérot-like cavity, the FSR includes an additional factor of two in

$$f_{FSR} = \frac{c}{2Ln}, \tag{3.5}$$

where the round trip of this passive cavity equals twice the length between the facet and the tip. Then, the free spectral range of this Fabry-Pérot cavity is shown in figure 3.19. We assume that most of the light is already lost from the cavity after the first reflection from the facet.

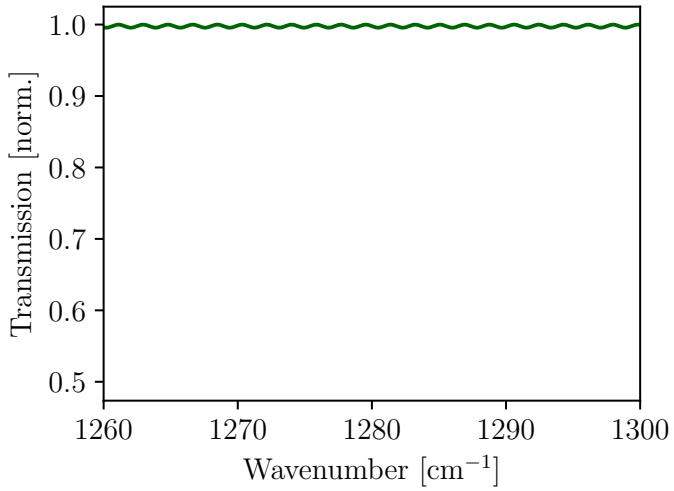

Figure 3.19: Free spectral range of the Fabry-Pérot-like cavity, which can be thought of as a high loss linear cavity in a passive medium between the tip of the egg laser and the facet.

To determine the lasing direction of the device, we combine the resonances of the cavities with the gain of the heterostructure, which in this case is centered around the wavenumber 1280 cm^{-1} and follows a Lorentzian lineshape, as shown in figure 3.20.

Finally, to choose the mode which experiences the higher net gain and thus dictates the lasing direction, the resonances from the two cavities, the circular cavity with a high quality factor, and the linear cavity between the tip of the device and the laser facet are combined with the modal gain of the heterostructure. Such a mode competition is illustrated in figure 3.21, where we can see that the gain of the laser narrows down the wavenumbers that could potentially win.

So far, we treated a symmetric system to build up the model, by decoupling the two lasing directions from each other and taking the same length for the linear cavities.

However, it is easy to imagine, that when cleaving the laser devices, we are not precise enough, such that the tip of the device is centered between the two facets. Therefore, we introduce a path difference between the two linear cavities, by shifting the tip of the device away from the center.

On top of that, the periodicity we have seen in the choice of the preferential lasing direction of the laser is a function of temperature. Therefore, to include a temperature

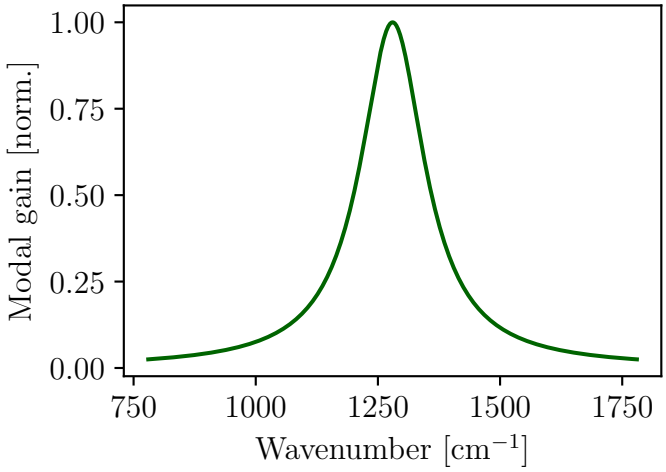

Figure 3.20: The gain of the layers EV2017, and EV2041 are similar to each other, they follow a Lorentzian lineshape, centered around the wavenumber 1280 cm^{-1}.

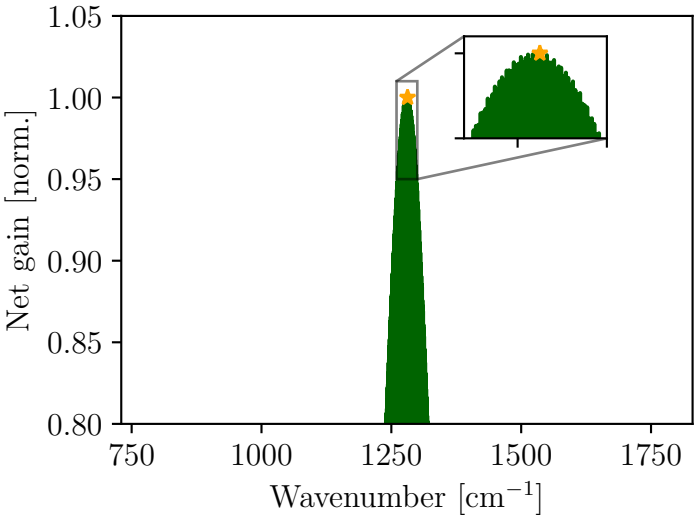

Figure 3.21: By including the contributions from the active, high quality factor, circular cavity, and the passive, low quality factor linear cavity, we treat the system as coupled cavities. In the wavelength region in which the gain of the layer overlaps with these resonances, the winner of the single mode emission can be chosen.

dependence in the model, we start to vary the refractive index of the InP cladding, assuming only a small linear change with temperature.

For a length difference of 200 µm between the linear cavities, we get a good qualitative agreement between the computations in figure 3.22 panel a) and the experimental data shown on panel b). At -20°C, the computation predicts a marginally higher net gain for the CW than the CCW direction, leading to preferred CW lasing after the symmetry breaking point. This prediction can be confirmed in the experimental data as a strong preference (i.e. a fully colored bar) at that temperature. As we move toward higher temperatures in

the simulation, the net gain of the CCW mode increases until it surpasses the CW gain at around -13°C. At that point, the preferred lasing direction switches; a behavior, that is also seen in the experiment. This switching occurs periodically within the computed and measured temperature ranges.

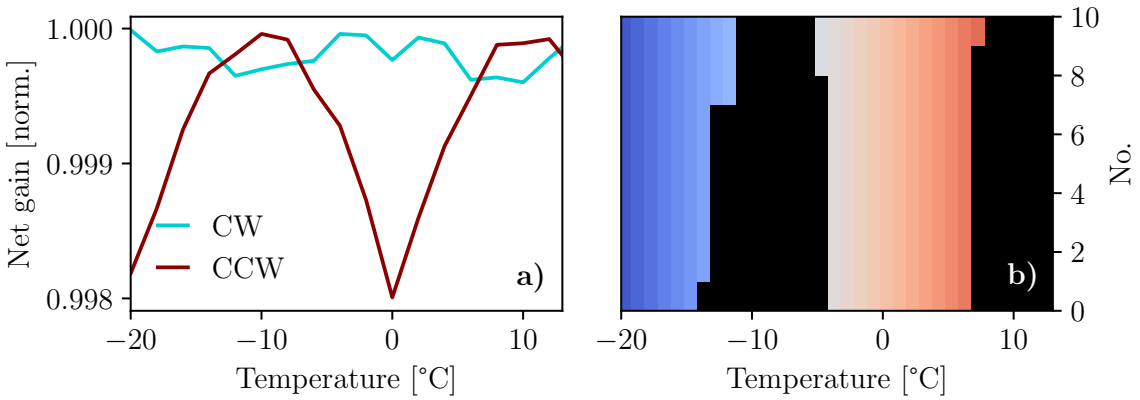

Figure 3.22: By shifting the tip of the egg from the middle, such that we don't have a symmetric system anymore, and varying the temperature through the refractive index of the InP cladding, the measurement results from panel b), same as figure 3.17 can be qualitatively reproduced with good accuracy.

Microscope images, shown in figure 3.23 confirm that in the case of the device measured, there was indeed a step in the facet, introduced by cleaving, which could lead to a shifted emission point of the laser from the middle. Since the laser was mounted epitaxial-side down, we are not able to extract the actual distances with which the tip is shifted from the center.

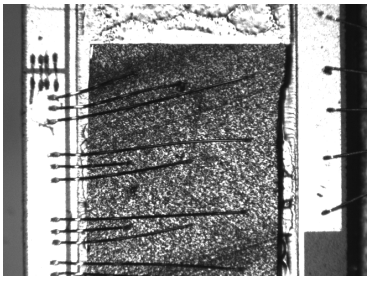

Figure 3.23: Epitaxial-side down mounted egg device, with a step in the facet on the side of the tip of the device, which could potentially cause the temperature-dependent symmetry-breaking behavior.

Even though this consideration of comparing the two directions to each other describes the behavior of the system qualitatively, we have to add a remark, that based on the measurements of the spectral identity of the modes, and the results from the HR coating state, the two lasing directions are inherently coupled to each other and cannot be treated separately, as reported in [8].

Chapter 4

Discussion and Outlook

In chapter 3, we attempted to address the main challenges of ring quantum cascade lasers, the low output power, and the inability to choose the lasing direction due to the spontaneous symmetry breaking of the devices.

To increase the performance of ring quantum cascade lasers, a modified design was employed with curvatures engineered such that the bending losses focus the emission of the device to a chosen point of the cavity. We studied both ring and egg quantum cascade lasers, and the outcome of the measurements could help design the next generation of circular laser devices to increase the output power. Furthermore, the performance of the egg lasers was increased by an anti-reflection coating applied on the front facets of the laser.

The anti-reflection coatings not only enhance the performance of the device but also help us deepen our understanding of the symmetry-breaking behavior of circular cavity lasers. We find that even though the reflections from the facet play an essential role and give some degree of control over the device when the laser is turned on nonadiabatically, it is not enough to drive the choice of lasing directions of circular cavity lasers consistently. However, for the integration of egg lasers, it is crucial to systematically choose the same lasing directions once the laser device is aligned. As a further step, following [39], optical seeding could be employed.

The importance of the feedback from the laser facet is also revealed by the highly reflective coating applied on the back facet of the laser because it leads to the conclusion that when we record the LI curves of ring and egg quantum cascade lasers, we measure a combination of both of the modes. However, as shown by the spectral identity of the two modes, they are not independent of each other. This supports a more physically accurate description of the laser devices with circular cavities.

Furthermore, based on the collaborative work with TU Munich [8], the relation between the backscattering and emission spectrum of lasers could help design tunable single-mode devices for high-resolution absorption spectroscopy applications [40]. In contrast to distributed feedback lasers [41], smooth quantum cascade laser ring cavities achieve stable single-mode emission without introducing selective losses into the cavity, potentially providing a novel mechanism for high-power monochromatic emission. Additionally, by anti-reflection coating, their backscattering coefficient could be further reduced to create an ideal platform for resonant injection.

Acknowledgement

First of all, I would like to thank Prof. Dr. Jérôme Faist for giving me the opportunity to perform and write this Master's thesis in his group, and Prof. Dr. Johan Chang for his approval and support in supervising my external thesis work.

Furthermore, I would like to express my gratitude to Ina Heckelmann, my direct supervisor, for her guidance and never-ending patience toward me.

Additionally, I would like to thank everyone from the Quantum Optoelectronics Group for the great time, and Dr. Mathieu Bertrand, Dr. Miguel Montesinos Ballester, Dr. Bahareh Marzban, Barbara Schneider, and Philipp Täschler for taking time out of their days to either help me fix measurements, or grasp theoretical concepts.

Last but not least, I would like to thank Bálint for helping and supporting me throughout my studies.

Bibliography

[1] A. Minotto *et al.*, "Visible light communication with efficient far-red/near-infrared polymer light-emitting diodes," *Light: Science & Applications*, vol. 9, p. 70, 2020.

[2] I. E. Gordon *et al.*, "The HITRAN2020 molecular spectroscopic database," *Journal of Quantitative Spectroscopy and Radiative Transfer*, vol. 277, p. 107 949, 2022.

[3] P. M. Hundt *et al.*, "Multi-species trace gas sensing with dual-wavelength QCLs," *Applied Physics B*, vol. 124, p. 108, 2018.

[4] P. Siegel, "Terahertz technology," *IEEE Transactions on Microwave Theory and Techniques*, vol. 50, pp. 910–928, 2002.

[5] T. H. Maiman, "Stimulated Optical Radiation in Ruby," *Nature*, vol. 187, pp. 493–494, 1960.

[6] B. Meng, M. Shahmohammadi, F. Kapsalidis, R. Wang, M. Beck, and J. Faist, "Mid-infrared frequency comb from a ring quantum cascade laser," *Optica*, vol. 7, pp. 162–167, 2020.

[7] B. Meng, M. Singleton, J. Hillbrand, M. Franckié, M. Beck, and J. Faist, "Dissipative Kerr solitons in semiconductor ring lasers," *Nature Photonics*, vol. 16, pp. 142–147, 2022.

[8] L. Seitner *et al.*, *Backscattering-Induced Kerr Solitons in Ring Quantum Cascade Lasers*, 2023. arXiv: `2304.07054 [physics]`.

[9] J. Faist, F. Capasso, D. Sivco, C. Sirtori, A. Hutchinson, and A. Cho, "Quantum Cascade Laser," *Science*, vol. 264, pp. 553–556, 1994.

[10] J. Faist, *Quantum Cascade Lasers*. Oxford: Oxford Academic, 2013.

[11] M. C. Tatham, J. F. Ryan, and C. T. Foxon, "Time-resolved Raman measurements of intersubband relaxation in GaAs quantum wells," *Physical Review Letters*, vol. 63, pp. 1637–1640, 1989.

[12] M. Beck *et al.*, "Continuous Wave Operation of a Mid-Infrared Semiconductor Laser at Room Temperature," *Science*, vol. 295, pp. 301–305, 2002.

[13] A. Gordon *et al.*, "Multimode regimes in quantum cascade lasers: From coherent instabilities to spatial hole burning," *Physical Review A*, vol. 77, p. 053 804, 2008.

[14] E. J. D'Angelo, E. Izaguirre, G. B. Mindlin, G. Huyet, L. Gil, and J. R. Tredicce, "Spatiotemporal dynamics of lasers in the presence of an imperfect O(2) symmetry," *Physical Review Letters*, vol. 68, pp. 3702–3705, 1992.

[15] B. Meng, M. Singleton, J. Hillbrand, M. Franckié, M. Beck, and J. Faist, "Dissipative Kerr solitons in semiconductor ring lasers (supplementary information)," *Nature Photonics*, vol. 16, pp. 142–147, 2022.

[16] M. Sorel, G. Giuliani, A. Scire, R. Miglierina, S. Donati, and P. Laybourn, "Operating regimes of GaAs-AlGaAs semiconductor ring lasers: Experiment and model," *IEEE Journal of Quantum Electronics*, vol. 39, pp. 1187–1195, 2003.

[17] H. Risken and K. Nummedal, "Self-Pulsing in Lasers," *Journal of Applied Physics*, vol. 39, pp. 4662–4672, 1968.

[18] R. Graham and H. Haken, "Quantum theory of light propagation in a fluctuating laser-active medium," *Zeitschrift für Physik A Hadrons and nuclei*, vol. 213, pp. 420–450, 1968.

[19] L. L. Columbo and M. Brambilla, "Multimode regimes in quantum cascade lasers with optical feedback," *Optics Express*, vol. 22, pp. 10 105–10 118, 2014.

[20] J. Faist *et al.*, "Quantum Cascade Laser Frequency Combs," *Nanophotonics*, vol. 5, pp. 272–291, 2016.

[21] A. Hugi, G. Villares, S. Blaser, H. C. Liu, and J. Faist, "Mid-infrared frequency comb based on a quantum cascade laser," *Nature*, vol. 492, pp. 229–233, 2012.

[22] T. Udem, R. Holzwarth, and T. W. Hänsch, "Optical frequency metrology," *Nature*, vol. 416, pp. 233–237, 2002.

[23] M. P. AG, *Frequency Combs*.

[24] P. Grelu and N. Akhmediev, "Dissipative solitons for mode-locked lasers," *Nature Photonics*, vol. 6, pp. 84–92, 2012.

[25] T. J. Kippenberg, A. L. Gaeta, M. Lipson, and M. L. Gorodetsky, "Dissipative Kerr solitons in optical microresonators," *Science*, vol. 361, eaan8083, 2018.

[26] P. Yeh, *Optical Waves in Layered Media* (Wiley Series in Pure and Applied Optics). New York: Wiley, 1988.

[27] P. Taeschler, "Injection-locking, external cavity beat-note control and output coupler design of THz quantum cascade laser frequency combs," Ph.D. dissertation, ETH Zurich, Switzerland, 2019.

[28] M. Jörger and G. Zachmann, "THE NEW VACUUM FT-IR SPECTROMETER: DESIGN ADVANCES AND RESEARCH APPLICATION,"

[29] R. Loudon, *The Quantum Theory of Light* (Oxford Science Publications), 3rd ed. Oxford ; New York: Oxford University Press, 2000.

[30] S. Riedi, "Broadband mid-Infrared Quantum Cascade Lasers for Spectroscopic Applications in External Cavity," Ph.D. dissertation, ETH Zurich, 2016, 146 p.

[31] H. Schmidbauer, "Eine exakte Eierkurvenkonstruktion mit technischen Anwendungen," *Elemente der Mathematik*, vol. III, pp. 67–68, 1948.

[32] I. Heckelmann, M. Bertrand, A. Dikopoltsev, M. Beck, G. Scalari, and J. Faist, "Quantum Walk Laser," 2023, unpublished.

[33] N. Opačak *et al.*, *Nozaki-Bekki optical solitons*, 2023. arXiv: `2304.10796 [nlin, physics:physics]`.

[34] P. Micheletti *et al.*, *THz optical solitons from dispersion-compensated antenna-coupled planarized ring quantum cascade lasers*, 2022. arXiv: 2211.07242 [physics].

[35] P. Malara *et al.*, "External ring-cavity quantum cascade lasers," *Applied Physics Letters*, vol. 102, p. 141 105, 2013.

[36] M. Piccardo *et al.*, "Frequency combs induced by phase turbulence," *Nature*, vol. 582, pp. 360–364, 2020.

[37] D. Kazakov *et al.*, "Defect-engineered ring laser harmonic frequency combs," *Optica*, vol. 8, pp. 1277–1280, 2021.

[38] L. Allen and J. H. Eberly, *Optical Resonance and Two-level Atoms*. Courier Corporation, 1987.

[39] S. Kacmoli, D. L. Sivco, and C. F. Gmachl, "Unidirectional mode selection in bistable quantum cascade ring lasers," *Optics Express*, vol. 30, pp. 47 475–47 484, 2022.

[40] E. Shim *et al.*, "Tunable single-mode chip-scale mid-infrared laser," *Communications Physics*, vol. 4, pp. 1–7, 2021.

[41] H. Kogelnik and C. V. Shank, "Coupled-Wave Theory of Distributed Feedback Lasers," *Journal of Applied Physics*, vol. 43, pp. 2327–2335, 1972.